THE ASTROPHYSICAL JOURNAL, 307:73–90, 1986 August 1

OBSERVATIONAL CONSTRAINTS ON BENDING THE WIDE-ANGLE TAILED RADIO GALAXY 1919+479

JACK O. BURNS
Institute for Astrophysics, University of New Mexico

CHRISTOPHER P. O'DEA
National Radio Astronomy Observatory[1]

STEPHEN A. GREGORY
Institute for Astrophysics, University of New Mexico

AND

THOMAS J. BALONEK
Institute for Astrophysics, University of New Mexico, and
Department of Physics and Astronomy, Colgate University
Received 1985 August 22; accepted 1986 January 20

ABSTRACT

New multiconfiguration VLA data at 18, 20, and 6 cm are presented for the 1 Mpc sized wide-angle tailed radio galaxy 1919+479. These radio maps, combined with photographic, optical CCD, and X-ray imaging data, are used to constrain models for bending the radio jets and tails. The 230 kpc stellar halo of the cD galaxy (identified with the compact radio core of 1919+479) suggests that the galaxy moves at less than 150 km s^{-1} within the cluster, otherwise this halo would be stripped by cluster-wide tidal forces. This low velocity, coupled with new limits on the radio source lifetime and energetics, argue against ram-pressure bending. The observed sharp bends in the jet and newly discovered counterjet strongly suggest that a transverse impulsive force is acting upon the plasma flows. We present a self-consistent jet/cloud collision model which bends the eastern jet via oblique shocks. A more dramatic, head-on collision with a cloud is considered for the counterjet. The nature of these intergalactic clouds is also described. Finally, we discuss generalizing this cloud collision model to all large wide-angle tails associated with cD galaxies.

Subject headings: galaxies: clustering — galaxies: individual — galaxies: jets — galaxies: structure — galaxies: X-rays — radio sources: galaxies

I. INTRODUCTION

Owen and Rudnick (1976) were the first to classify tailed radio sources in rich clusters into two categories according to the degree of bending and the luminosity. Wide-angle tails (WAT) have greater than 90° angles between the tails. WATs also have 1.4 GHz powers intermediate between classical doubles and narrow-angle tailed (NAT) sources (e.g., O'Dea and Owen 1985), $P_{1.4} \approx 5 \times 10^{24}$ W Hz^{-1}. The classic example is 3C 465 (see, e.g., Eilek *et al.* 1984). All members of this class are associated with a dominant galaxy in a cluster. A subset, such as 3C 465 and 1919+479, is identified with supermassive cD galaxies located at the optical and X-ray centers of rich clusters.

Burns, Eilek, and Owen (1982) and Burns (1983, 1986) have identified the problems with bending WATs as a result of their association with dominant, slowly moving cluster galaxies. Unlike the NATs, there is insufficient dynamic pressure available to bend the radio structure, given the jet momentum flux needed to power the tails. Eilek *et al.* (1984) considered a wide range of possible alternative mechanisms, including jet/cloud collisions and electrodynamic Lorentz forces, but were unable to settle on a single best model for 3C 465. There is a need for more detailed observations of other examples of the WAT class to illuminate the bending mechanism.

Burns and Owen (1979) serendipitously recognized the rich cluster WAT source 1919+479 (4C 47.51) while surveying poor clusters at radio frequencies. Initial reports of the structure by Robertson (1980, 1984) using Westerbork (WSRT) and by Burns (1981) using the precompletion VLA showed it to be the largest known example of a WAT. At a redshift of 0.104 (Gregory and Burns 1982), corresponding to a distance of 359 Mpc using $H_0 = 75$ km s^{-1} Mpc^{-1} and $q_0 = 0$ (used throughout this paper), its overall linear extent (in projection) exceeds 1 Mpc.

The radio galaxy 1919+479 is both the most extreme and the simplest example of this morphology class. It is extreme in its lifetime and corresponding energy requirements because of the distance from the galaxy over which plasma must flow, and extreme in the degree of bending. It is the simplest in terms of the optical environment. The optical galaxy is clearly a very dominant, single nucleus cD galaxy located within the single dominant concentration of galaxies in a moderately rich cluster (see § III). This environment eliminates complications in bending models which may involve motions of multiple nuclei or multiple subcondensations in a highly evolving cluster. Therefore, 1919+479 presents possibly the best example for further study of the WAT problem.

In this paper, we present a wide range of new observations of 1919+479 and its environs. In § II, multifrequency and multifiguration VLA observations are described, ranging in resolution from 0".7 to 40". Distributions of source structures at different scale sizes, spectral indices, and polarizations are presented. In § III, wide-field photographic and CCD imaging

[1] Operated by Associated Universities, Inc., under contract with the National Science Foundation.

data are presented, along with a review of the measured galaxy redshifts in the field. In § IV, we show a newly reprocessed *Einstein* IPC X-ray image of the cluster and describe the X-ray emission's relationship to the radio morphology. In § V, the radio, optical, and X-ray data are used to constrain the cD galaxy dynamics and models for bending the radio structure. In particular, we consider the possible role of jet collisions with clouds in the intracluster medium (ICM). Finally, in § VI, we summarize the results and discuss the applicability of cloud collision models to WATs in general.

II. VLA RADIO DATA

a) Log of the Observations

Previous observations of 1919+479 have shown that the radio source is $\sim 10'$ in extent and is rich with substructure. In order that all scale sizes of structure should be properly sampled at (a minimum of) two frequencies and in linear polarization, as well as total intensity, observations of 1919+479 were performed in all four VLA configurations. A log of these observations is presented in Table 1, along with a guide to the radio source maps.

b) Observations and Data Reduction

Generally, 12 hr observations of 1919+479 in each VLA configuration were performed. We alternated between 4.9 GHz (6 cm) and 1.5 GHz (20 cm) about every 20 minutes with appropriate calibrator observations in between. In addition, 1.7 GHz (18 cm) observations in the B-configuration were made in an attempt to sort out Faraday rotation effects in the radio tails. Bandwidths of 25 MHz were used throughout the observations. Further details of the VLA can be found in Thompson *et al.* (1980).

The data were calibrated in the usual fashion following the procedures outlined in Hjellming (1982). The source fluxes were normalized to the Baars *et al.* (1977) scale, and polarization position angles were calibrated using observations of 3C 286. These calibrated visibilities were then processed using the NRAO AIPS computer package. The visibilities were Fourier transformed into "dirty" maps, and these maps were CLEANed of sidelobes using the Clark (1980) implementation of the CLEAN algorithm. Self-calibration (e.g., Schwab 1980) was also performed on the A-configuration, high-resolution data which raised the dynamic range by a factor of 2 on the final maps. Primary beam corrections were applied to the 6 cm wide-field maps.

TABLE 1

LOG OF VLA OBSERVATIONS

Date	VLA Configuration	λ (cm)	ν (MHz)	Phase Center RA (1950) Decl. (1950)	Figures
1982 Jan 16	C	6	4873	$19^h19^m49\overset{s}{.}28$	5–8
		20	1418	$47°59'00\overset{''}{.}0$	1, 2, 5–8
1982 Feb 23	A	6	4886	$19^h19^m49\overset{s}{.}93$	4
		20	1446	$48°00'32\overset{''}{.}9$	1
1982 Aug 8	B	6	4873	$19^h19^m49\overset{s}{.}28$	4
				$47°59'00\overset{''}{.}0$	...
1982 Oct 3	B	18	1652	$19^h19^m49\overset{s}{.}28$	...
		20	1418	$47°59'00\overset{''}{.}0$	1, 2, 5–8
1983 Jul 7	D	6	4873	$19^h19^m49\overset{s}{.}78$	5–8
		20	1418	$47°59'00\overset{''}{.}0$	9

c) Overall Source Morphology

Excellent views of both the small- and large-scale structures associated with 1919+479 at 20 cm are shown in Figures 1*a* (Plate 1) 1*b*, and 2 (Plate 2). The maps in Figure 1 were produced by combining data from both high (A-configuration) and moderate (B-, C-configurations) resolutions, tapering the resulting visibilities, and restoring the map with a Gaussian clean beam of $4\overset{''}{.}5$ FWHM. Figure 2 is a lower resolution map with a circular beam of 13" FWHM constructed from C-array data.

As previously noted by Burns (1981) and Robertson (1980, 1984), the radio structure of 1919+479 is remarkably asymmetric on opposite sides of the optical galaxy (optical galaxy coincides with the bright, western-most knot in the jet; see below). The eastern side of the source consists of a gently curved, clumpy jet which bends and dramatically expands into a diffuse lobe. At a redshift of 0.104 (1" = 1.74 kpc), the eastern structure has a total projected extent (measured from the galaxy) of 680 kpc.

The western side of the source consists of a very different radio morphology, with a prominent, wiggling tail oriented in a north-south direction. The tail contains significant variations in width along its total extent of 800 kpc.

A plot of the deconvolved FWHM widths of both tails as a function of distance from the galaxy is shown in Figure 3. These widths were determined from Gaussian fits to the cross-sectional profiles. The apparent expansion and recollimation in the tails are reminiscent of those seen in radio jets (e.g., Bridle 1982). Interpretation of the oscillations in width is offered in § V.

These new observations have revealed the presence of a weak counterjet which extends from the galaxy core to a resolved hot spot (position 7 in Fig. 1*b*) to the northwest. This counterjet is best seen on the lower resolution map in Figure 2. The apparent bend of greater than 90° between the counterjet and the tail is curious, adding to the uncertainty concerning the mechanism responsible for bending the overall structure.

The three other, more compact sources seen in this field are not associated with the radio galaxy or the surrounding cluster. They are identified with background objects.

Table 2 contains a listing of some of the major properties of the source features seen in Figure 1. The minimum pressure calculations were performed following the prescription discussed in Burns, Owen, and Rudnick (1978). The jet and tail components were taken to have cylindrical symmetry, and the calculations were performed on a single beamwidth projected along the line of sight through the source. We also assumed equal energies in electrons and protons, a magnetic field filling factor of 1, and a power-law radiation spectrum (spectral indices listed in Table 2) extending between 10 MHz and 100 GHz.

d) High-Resolution Radio Maps

Figure 4 (Plate 3) contains our highest resolution map of 1919+479 convolved with a circular Gaussian clean beam of $0\overset{''}{.}67$ FWHM. The visibility data base from which this map was made consists of both A- and B-array observations at 6 cm.

There are no structures visible in this map located within the western tail. All features, including the hot spots (positions 5 and 7; see Figs. 1 and 2), are completely resolved at this resolution.

However, there is a wealth of compact structure within the eastern jet. There are at least five individual features which we

FIG. 1*a*.—Gray-scale VLA image of 1919+479 at 20 cm

BURNS, O'DEA, GREGORY, AND BALONEK (*see* page 74)

1986ApJ...307...73B

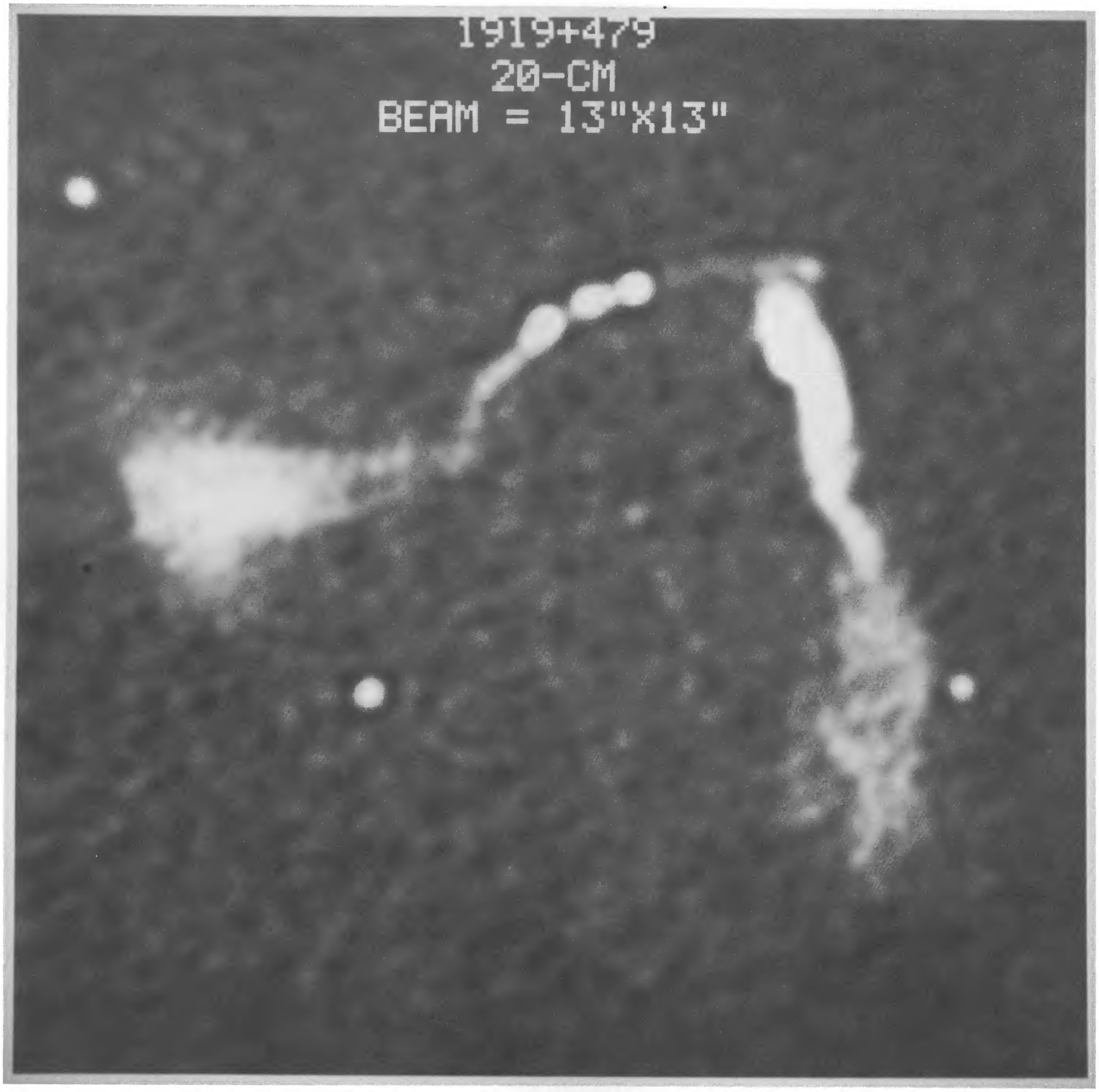

FIG. 2.—Gray-Scale, 13″ resolution VLA image of 1919+479. Note the counterjet and its orientation perpendicular to the western radio tail.

BURNS, O'DEA, GREGORY, AND BALONEK (*see* page 74)

1986ApJ...307...73B

FIG. 4.—Highest resolution VLA image of the eastern jet in 1919+479. Note the sharp bends at the brightest knots.

BURNS, O'DEA, GREGORY, AND BALONEK (*see* page 74)

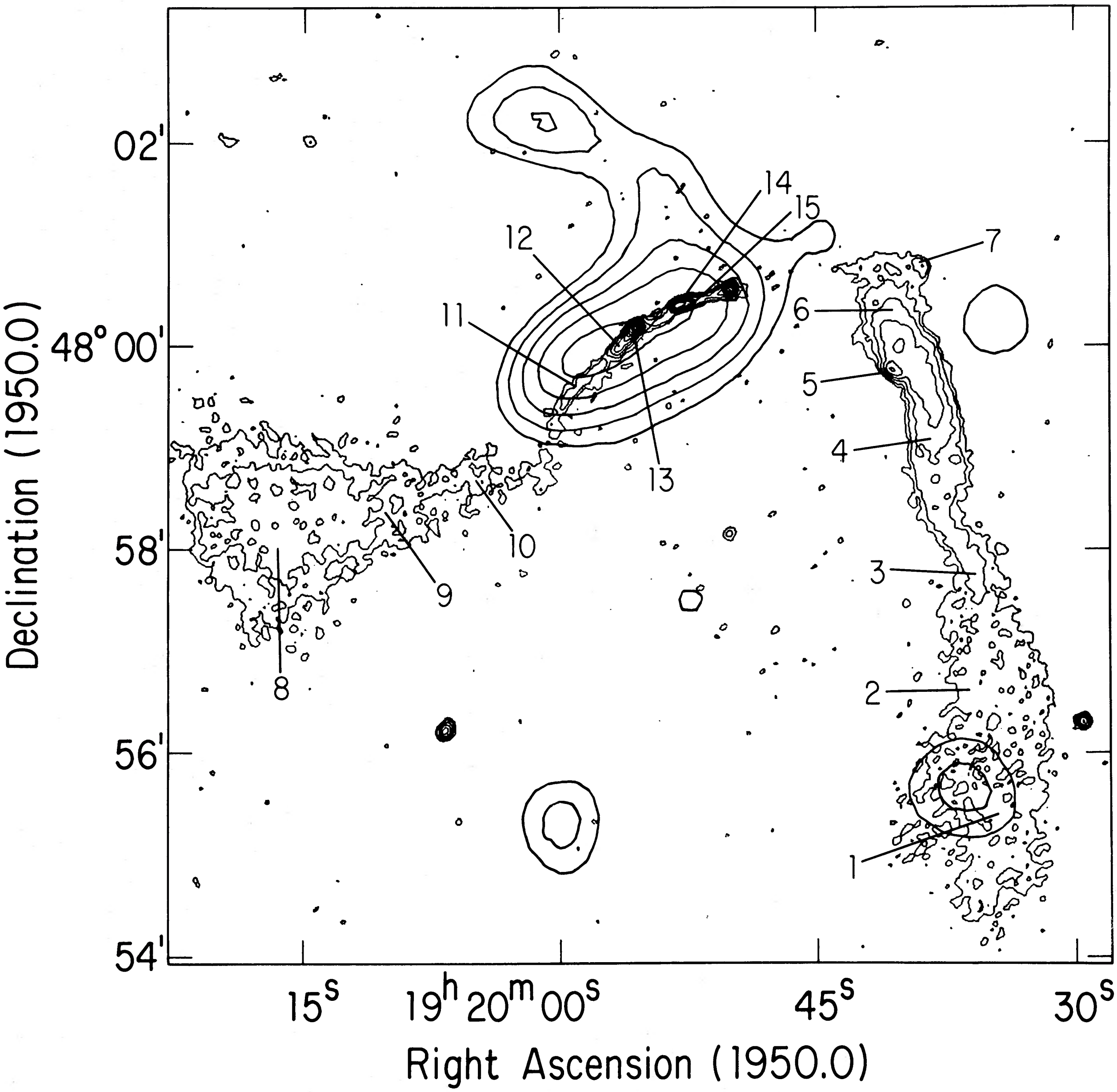

FIG. 1b

FIG. 1b.—Radio and X-ray contours of emissions. Fine-line contours are the 20 cm radio emission shown in Fig. 1a; contour levels are −0.3, 0.3, 0.6, 1.2, 2.2, 3.4, 5.0, 6.8, 9.0, 11.5, 14.3, 17.4, 20.2, 24.5, 28.5, and 32.9 mJy per beam. Bold contours represent the IPC X-ray emission at a resolution of 1'.8; contour levels (in arbitrary units) are 53%, 64%, 74%, 85%, and 96% of the peak.

identify as knots within the jet. The four brightest knots all appear to be resolved at this resolution with transverse FWHM values ranging from 0''.6 (1.0 kpc) to 1''.2 (2.1 kpc), as determined by two-dimensional Gaussian fits. These high-resolution data were used to determine the minimum jet pressures in Table 2.

This resolution demonstrates that the jet in 1919+479 is not a smooth, continuously curving structure. Instead, there are several sharp southward-leading bends which occur at the locations of the brightest jet knots (particularly at position 13 in Fig. 1b). The jet gently bows to the south initially, peaking at knot 14. Between 14 and 13, there is a stronger bow to the south. At knot 13, there is a dramatic, sharp bend again to the south. After knot 13, there are no further knots and the jet begins to lose collimation rapidly. This structure is quite different from the continuously bent U-shaped head-tail sources (e.g., O'Dea and Owen 1985) such as 3C 129 (Rudnick and Burns 1981). Sharp bends in jet structures appear to be a common feature among the WAT sources including 3C 465 (Eilek *et al.* 1984). Such bends must be a clue to the mechanism responsible for shaping the WAT structure.

e) Moderate Resolution Data

Figures 5–8 present maps of 1919+479 at resolutions of 4'' and 10'', at 20 and 6 cm wavelengths. These maps were constructed from visibility data bases containing B- and C-array observations at 20 cm, and C- and D-array observations at 6 cm. Therefore, the $u-v$ coverages and resolutions at the two

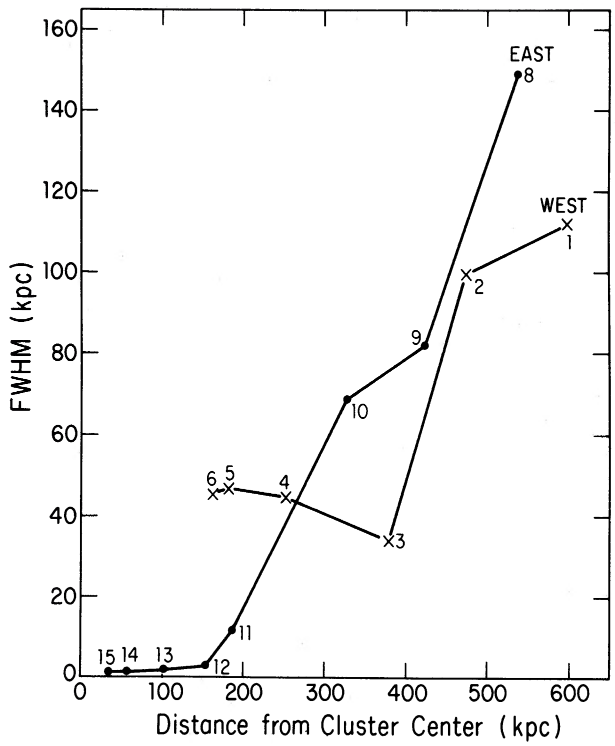

FIG. 3.—Distribution of source component widths as a function of distance from the cluster center (position of cD galaxy)

frequencies are nearly identical. These sets of equal resolution maps allow us to examine the distributions of spectral index, depolarization, and Faraday rotation within the source. The visibilities were tapered to two different resolutions so that we could examine the multiwavelength parameters of a wide range of scale sizes of structure.

In addition, maps at 4″ resolution were produced at 18 cm wavelength (not shown here). With these data, three-frequency percentage polarizations and **E** vector position angles could be determined.

i) *Spectral Indices*

Gray scale maps of spectral index, α (where $S \propto \upsilon^{+\alpha}$), between 20 and 6 cm are shown superposed upon contour plots of total intensity at 20 cm in Figures 5*a* and 5*b* at 10″ resolution. Regions of flatter spectral index are darker. The spectral index is shown only where its 1 σ error (using the rms noise at the primary beam center) is less than 0.15 in Figures 5*a* and *b*. Fuurther from the primary beam center, the attenuation at 6 cm results in a larger maximum error in α. Representative values of the spectral index are shown in the figures and are also listed in Table 2 for the positions defined in Figure 1*b*. The gray scale in Figure 5*b* displays $-0.5 \geq \alpha \geq -1.0$ and thus emphasizes regions of flatter spectral index in the diffuse structure.

Note that since the source is so large in angular extent, the effects of "bandwidth smearing" (e.g., Thompson 1982) can be significant. At a distance of 5′ from the phase center, a 25 MHz bandwidth and a 10″ beam result in a beam broadening of ~2% at 6 cm and 10% at 20 cm. Since the source will then appear larger at 20 cm, this will have the effect of artificially steepening the spectral index at the edges of the source; therefore such steepenings should be viewed with caution. Flattenings of the spectral index at the edges of the source should not be caused by this effect and are more likely to be real.

The eastern jet out to just beyond the second bright knot (position 12 in Fig. 1*b*) has a rather flat spectral index of −0.58 (Fig. 5*a*) which is typical of radio jets (e.g., Bridle and Perley 1984). The general steepening of the spectra with distance from the core is entirely consistent with the low-resolution (26″ × 35″) maps presented by Robertson (1984).

The 10″ resolution data reveal additional spectral index structure. In the eastern lobe (Fig. 5*b*), there is a coherent ridge of flatter spectral index (−0.8 to −0.9) which extends eastward

TABLE 2

RADIO SOURCE COMPONENT PROPERTIES

Region[a]	S (mJy)[b]	α_6^{20}[c]	FWHM[d]	B (μG)[e]	P (dyn cm^{-2})[f]	t (yr)[g]
1...........	0.5	-1.17 ± 0.10	64″.6	2.0	3.2×10^{-13}	8.2×10^7
2...........	0.6	-1.29 ± 0.08	57.3	2.1	3.7×10^{-13}	7.9×10^7
3...........	0.8	-0.90 ± 0.09	19.4	2.4	4.8×10^{-13}	7.4×10^7
4...........	1.4	-0.86 ± 0.06	25.5	2.5	5.3×10^{-13}	7.2×10^7
5...........	3.7	-0.62 ± 0.03	26.7	2.9	7.1×10^{-13}	6.5×10^7
6...........	1.5	-0.73 ± 0.05	26.4	2.3	4.5×10^{-13}	7.5×10^7
7...........	0.3	-0.51 ± 0.09	4.4	4.2	1.4×10^{-12}	4.6×10^7
8...........	1.0	-1.01 ± 0.05	81.0	1.9	2.9×10^{-13}	8.3×10^7
9...........	0.6	-1.02 ± 0.14	47.0	1.9	3.0×10^{-13}	8.3×10^7
10...........	0.4	-1.04 ± 0.13	39.8	1.8	2.6×10^{-13}	8.5×10^7
11...........	0.8	-0.76 ± 0.07	7.0	2.8	6.8×10^{-13}	6.6×10^7
12...........	0.3*	-0.55 ± 0.04	1.3	12.0	1.3×10^{-11}	1.1×10^7
13...........	0.5*	-0.57 ± 0.01	1.2	14.0	3.6×10^{-11}	4.6×10^6
14...........	2.9*	-0.61 ± 0.02	0.6	22.0	4.1×10^{-11}	4.7×10^6
15...........	2.3*	-0.58 ± 0.04	0.7	19.0	3.1×10^{-11}	5.8×10^6

[a] Region refers to Fig. 1*b*.

[b] Flux density at peak of cross-sectional cut through source structure. Flux densities were measured at 20 cm from Fig. 1*b*, except those values with a "*" which were measured at 6 cm from Fig. 4.

[c] Spectral index defined by $S_\nu \propto \nu^\alpha$.

[d] Full width at half-maximum determined from Gaussian fits of the one dimensional profiles (deconvolved from beam).

[e] Magnetic field strength assuming minimum pressure conditions.

[f] Minimum internal component pressure.

[g] Source component lifetime including synchrotron and inverse Compton losses.

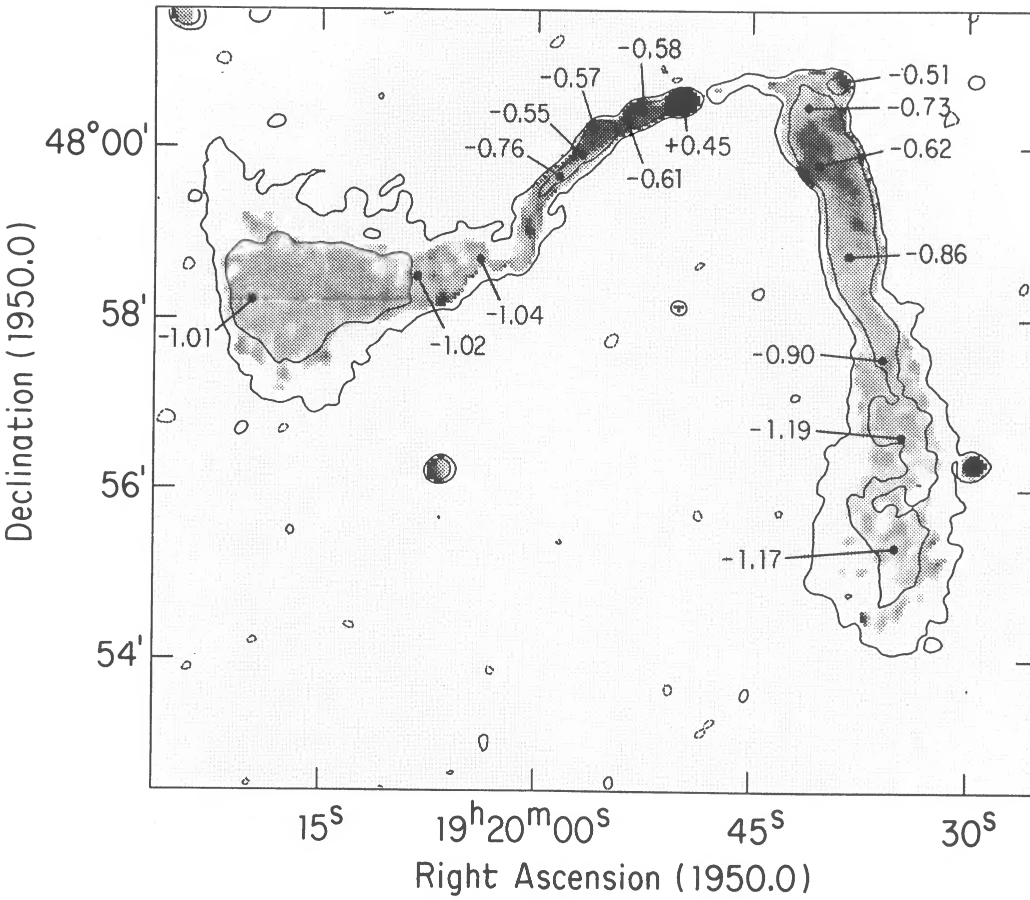

FIG. 5*a*

FIG. 5.—Distribution of 6–20 cm spectral indices (gray-scale) with total intensity contours overlaid. Fig. 5*a* illustrates a broad range of spectral indices (ranging from −0.4 (*darkest*), to −1.5 (*lightest*). Fig. 5*b* emphasizes the flatter α_6^{20} values ranging from −0.5 (*darkest*) to −1.0 (*lightest*). Resolution in both maps is 10″. Contour levels of total intensity are −0.5%, 0.5%, and 2% of 100 mJy per beam.

into the lobe from a feature on the southern edge of the lobe (−0.58).

The flattenings in the spectra allow a determination of the location of sites of local particle acceleration. The data presented above suggest that such reacceleration occurs in the following locations:

1) In the hot spot at the end of the counterjet ($\alpha \approx -0.5$);

2) In the hot spot at position 5 in the western tail ($\alpha \approx -0.5$);

3) In the eastern jet as it enters the lobe ($\alpha \approx -0.58$);

4) Possibly in the bright knots in the eastern jet ($\alpha \approx -0.58$).

On the other hand, the global steepening of the spectra (from about −0.7 to −1.2; Fig. 5*b*) in the western tail allows a determination of the ages of the radiating electrons (subject to some assumptions). For this purpose, we will use the results of Meyers and Spangler (1985), who examined the effects of synchrotron losses on the spectrum of the electron population for two different limiting cases of the distribution of the electron pitch angles. A conservative estimate of the electron age is obtained using Figure 2 of Meyers and Spangler, taking initial and final spectral indices of −0.75 and −1.2, respectively, (minimum pressure; see Table 2) and magnetic field of 2 μG, and an isotropic pitch-angle distribution. This gives an estimate of the electron age of 10^8 yr which is not very sensitive to the input parameters; i.e., using a flatter initial spectral index or a constant pitch angle distribution increases the age by no more than a factor of 2. This estimate ignores adiabatic losses; however, this age is in rough agreement with the synchrotron and inverse Compton lifetimes given in Table 2, suggesting that adiabatic losses have not been very important. This age is made a lower limit to the age of the radio source if reacceleration has occurred. The implications of this age for models of 1919+479 are discussed in § V.

ii) *Rotation Measure*

The rotation measure (RM) was calculated using a least-squares fit to the position angles at 20, 18 (B-configuration), and 6 cm (C-configuration) at 4″ resolution. The RM was calculated only where the signal to noise (S/N) in polarized flux density was greater than 3 at all three wavelengths. The position angles (χ) are well described by a $\chi \propto \lambda^2$ relationship. The use of three wavelengths (with two of them close together) allows a reasonably unambiguous determination of the RM.

A gray-scale map of RM is shown superposed on contours of polarized intensity in Figure 6. Regions of more positive RM are darker. Because of the high resolution of the maps, only the brightest parts of the eastern jet and western tail are seen in Figure 6*a*.

The RM ranges between roughly −65 and +5 rad m^{-2}. A

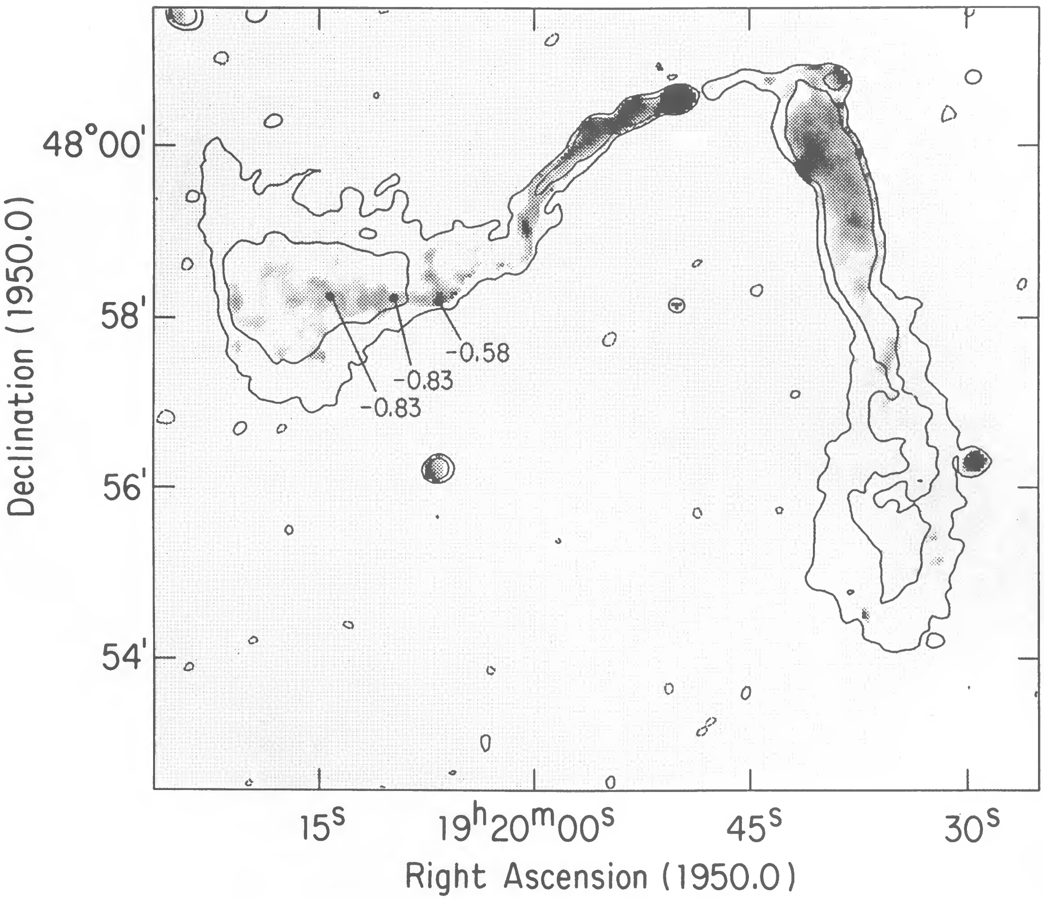

FIG. 5*b*

search for very large values of RM was carried out using a computer program (constructed as described by, e.g., Vallée and Bignell 1983) which searched values of RM between 10^3 to -10^3 in steps of 5 rad m^{-2} in selected regions. The observed position angles are entirely consistent with the small negative values of RM found here.

This range of RM values is significantly different from the global value of $\sim$150–300 rad m^{-2} found for the general area near 1919+479 ($l = 70\overset{\circ}{.}6$, $b = 15\overset{\circ}{.}2$; Simard-Normandin, Kronberg, and Button 1981). The upper limit to the RM contribution from 1919+479 derived by assuming that all of the observed depolarization is produced internally [see § II*e*(v)] is $\sim$30–40 rad m^{-2} and is thus too low to account for the difference. The S/N in polarization of the three background sources is too low for them to be useful in determining the contribution from the 1919+479 cluster to the total RM. However, in general, rich clusters of galaxies have RMs of order 50 rad m^{-2} (e.g., Dennison 1979) which is also too low to account for the difference. The remaining possibility is that the RM differences are Galactic in origin. This is supported by the following: (1) variations in Galactic RM of order the necessary 200 rad m^{-2} over angular size scales of degrees are observed (e.g., Simard-Normandin and Kronberg 1980). (2) There is a slight "hole" in the Galactic H I distribution in the direction of 1919+479 (Heiles 1975).

The RM is patchy, i.e., there are apparently random variations of order 10 rad m^{-2} over size scales of order 10″ (Fig. 6*a*). Since the 1 σ errors in the fitted RM are $\sim$1–2 rad m^{-2}, these variations are significant. There is a tendency for the RM to vary preferentially across the western tail; however, this is not confirmed by the lower resolution data (see below). The largest such variation occurs near the top of the western tail where the RM varies from about -40 rad m^{-2} on the east edge to about $+5$ rad m^{-2} on the west edge (Fig. 6*a*).

The RM on larger scales at 10″ resolution (Fig. 6*b*) was calculated using only two wavelengths (20 cm B+C configurations and 6 cm C+D). Because of the $n\pi$ ambiguity in the position angles it was assumed that the RM is smoothly continuous with that seen at higher resolution (Fig. 6*a*) and that there are no discontinuous jumps in RM.

At low resolution, there are variations of up to $\sim$40 rad m^{-2} over size scales of 1′, confirming the suggestion of patchiness in the RM. The largest variations in RM occur in roughly the top third of the western tail. The RM in this region also tends to differ systematically by $\sim$20 rad m^{-2} from that in the lower part of the tail. There are variations of $\sim \pm 10$ rad m^{-2} but no systematic trends in RM along the eastern jet. The east lobe has a fairly steady RM of about -44 rad m^{-2} with little variation across the lobe.

There is not a large systematic difference in RM between the eastern and western sides of the source (Fig. 6*b*), so, if a foreground screen in responsible for the bulk of the RM, it does not vary significantly (i.e., by more than $\sim$10 rad m^{-2}) on a scale of $\sim$6′.

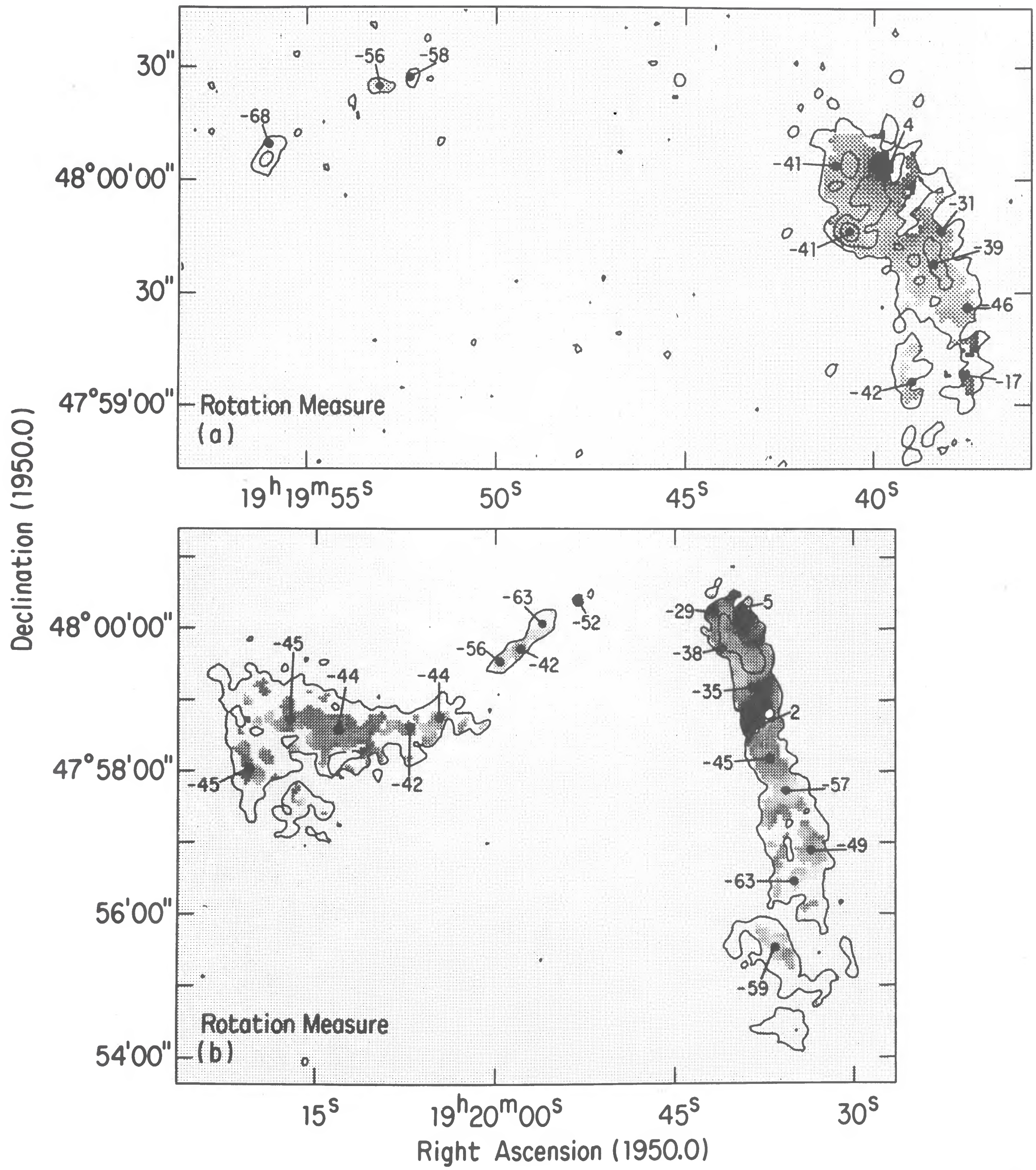

FIG. 6.—Distribution of 6–20 cm rotation measure (RM) with contours of polarized intensity overlaid. (*a*) 4" resolution gray-scale display of RM with values ranging from $+10$ rad m^{-2} (*darkest*) to -60 rad m^{-2} (*lightest*). Contour levels are 3.0%, 7.0%, and 12.0% of 10 mJy per beam. (*b*) 10" resolution gray-scale display of RM with values ranging from $+10$ rad m^{-2} (*darkest*) to -65 rad m^{-2} (*lightest*). Contour levels are 3.0% and 20.0% of 20 mJy per beam.

iii) *Magnetic Field Structure*

The global structure of the ***E*** vectors at 20 and 6 cm (10" resolution) is shown in Figures 7*a* and 7*b*. Since the RM is generally small, the net position angle rotation at 6 cm will be only a few degrees. Thus, the apparent projected (synchrotron emissivity weighted) ***B*** field will be approximately orthogonal to the ***E*** vectors at 6 cm (Fig. 7*b*).

The ***B*** field in the eastern jet is parallel to the jet axis all along the length of the jet. This is in contrast to what is generally seen in edge-darkened sources (e.g., Bridle and Perley 1984) but is consistent with observations of bent jets in other tailed sources (e.g., Burns 1983; O'Dea and Owen 1986).

In the western tail, the ***B*** field is parallel to the axis and seems to follow the wiggles in the source structure. There is also a high degree of order in the ***B*** field. The ***B*** field in the eastern tail is apparently circumferential; i.e., it is aligned with

1986ApJ...307...73B

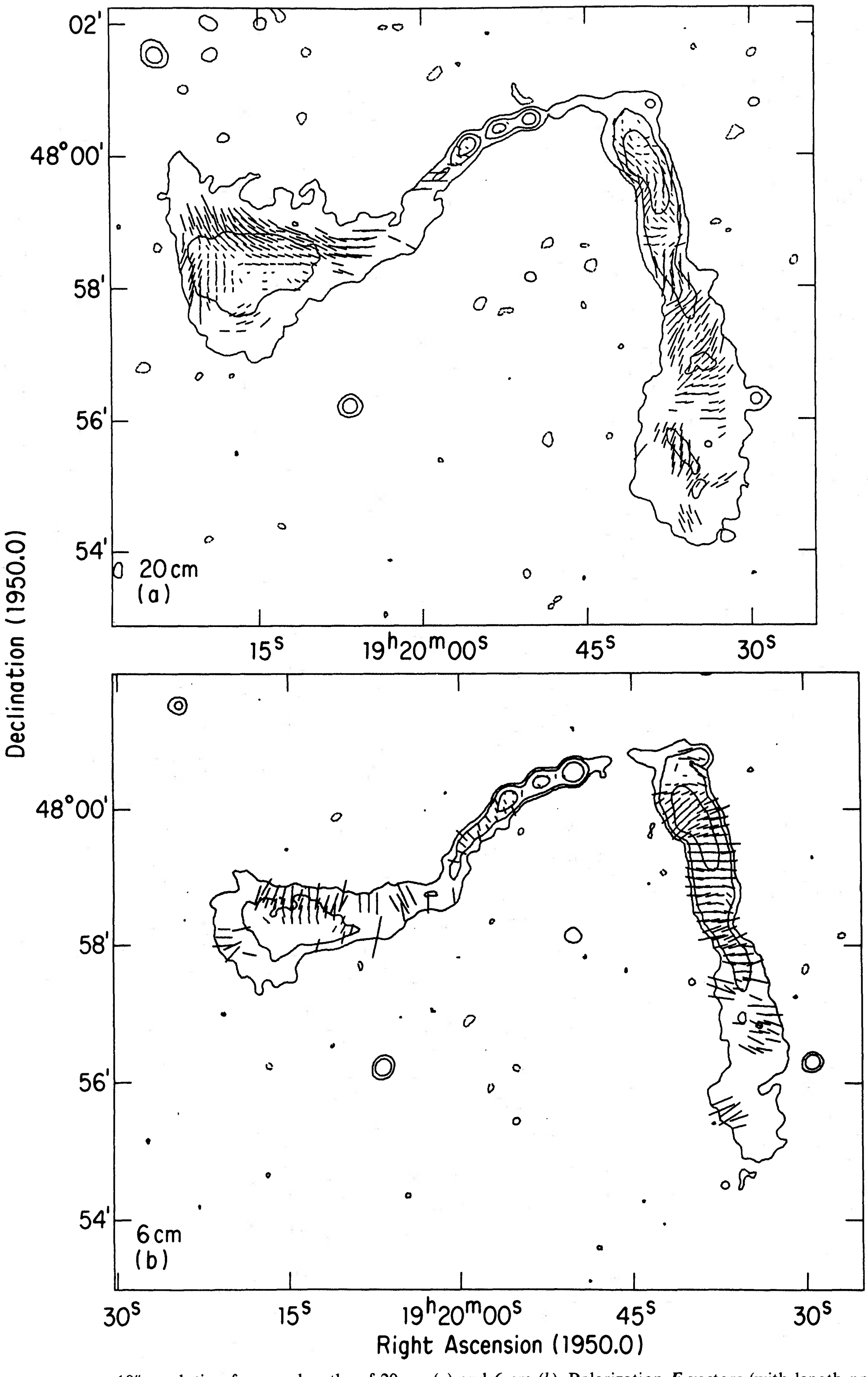

FIG. 7.—Total intensity contours at 10″ resolution for wavelengths of 20 cm (*a*) and 6 cm (*b*). Polarization ***E*** vectors (with length proportional to fractional polarization) are superposed on the contours. Contour levels are −0.5%, 0.5%, 2.5%, and 8% of 100 mJy per beam in (*a*). Contour levels are −1.5%, 1.5%, 5%, and 30% of 10 mJy per beam in (*b*).

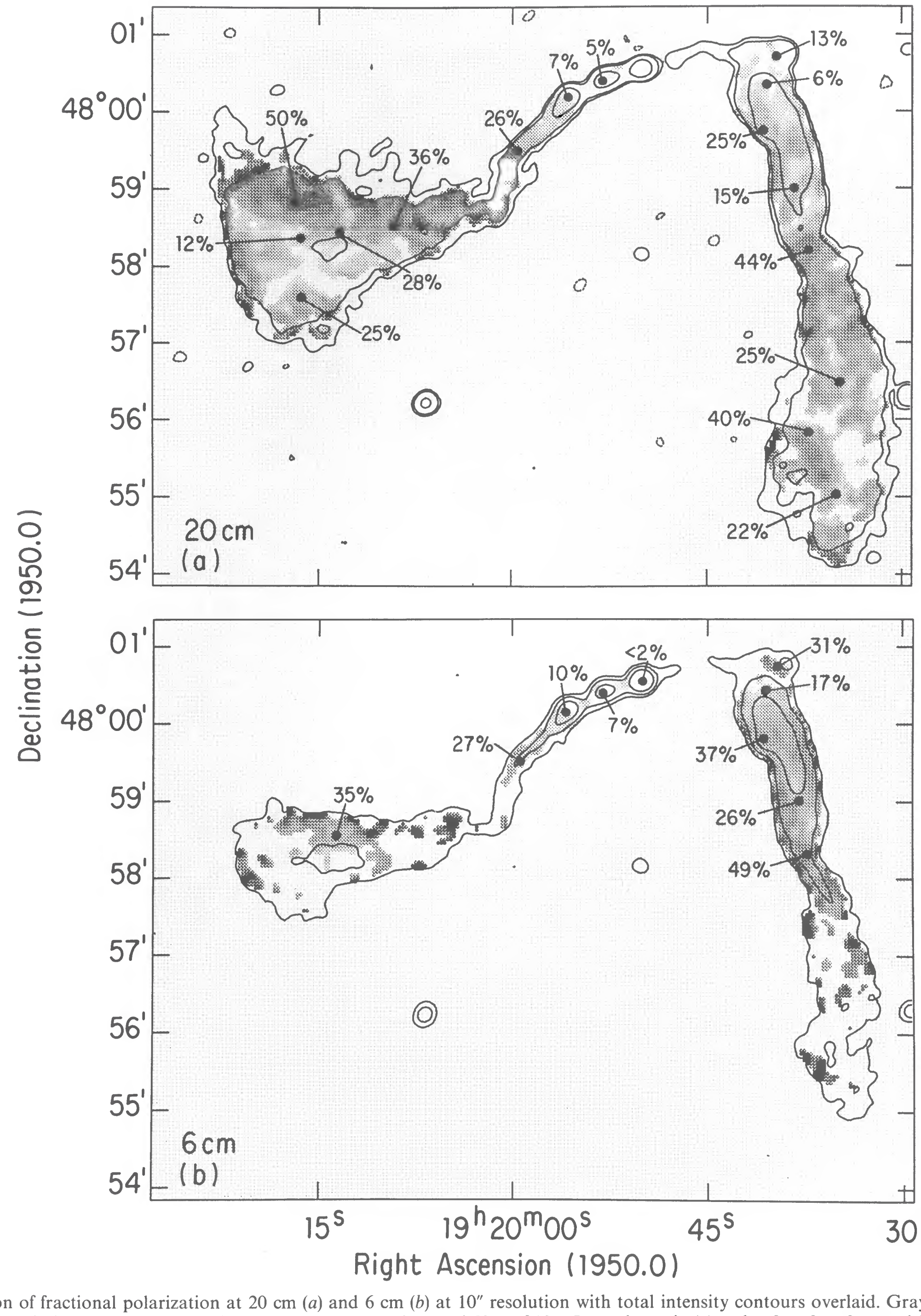

FIG. 8.—Distribution of fractional polarization at 20 cm (*a*) and 6 cm (*b*) at 10″ resolution with total intensity contours overlaid. Gray levels range from 80% (*darkest*) to <1% (*lightest*) in both maps. Contour levels are −5%, 5%, 10%, and 50% of 10 mJy per beam in (*a*) and −2%, 2%, 8%, and 30% of 10 mJy per beam in (*b*).

the edges of the source. Because of the low S/N in fractional polarization at the southern edge only a few ***E*** vectors are seen at the southern edge. Thus, this result must be viewed as tentative.

iv) *Fractional Polarization Structure*

The positive bias was removed from the polarized intensity (Wardle and Kronberg 1974), and maps of fractional polarization (shown only where the S/N > 3) were made (Fig. 8*a*, *b*). The gray scale is shown superposed on contours of total intensity. Representative values of the fractional polarization are shown in selected locations. Some of the high peaks in fractional polarization at the very edges of the source are probably spurious.

At 6 cm (Fig. 8*b*) the basic results are the following. The fractional polarization of the eastern jet is ~10% near the core and increases to ~25%–30% near the lobe. There is a suggestion that the eastern lobe is edge brightened, with values increasing from $\sim 20\%$ in the center to $\sim 40\%$–50% closer to the edges (particularly the northern and southeastern edges). The fractional polarization increases along the western tail from $\sim 20\%$ near the top to $\sim 40\%$–50% at $\sim 3'$ down the tail. There are no significant gradients or edge brightning across the western tail.

At 20 cm (Fig. 8*b*) the S/N is somewhat higher, and a larger portion of the source is seen with S/N > 3. The same global trends in fractional polarization are seen, although the values at 20 cm are systematically lower than at 6 cm.

v) *Depolarization*

The fractional polarization at 6 cm at 4″ and 10″ resolution are comparable. At 20 cm, however, the fractional polarization at 4″ is higher than at 10″ resolution (for those parts of the source which are seen in the lower surface brightness sensitivity maps at 4″ resolution). In general, the fractional polarization at 20 cm is lower than at 6 cm; i.e., there is depolarization throughout the source.

At both resolutions, the depolarization ratio ($P_{20/6}$) is somewhat "patchy," but the global structure is as follows. At 4″ resolution, $P_{20/6} \approx 0.7$–0.9 along the eastern jet near the knots and ~ 0.5–0.8 in the upper portions of the western tail. At the lower resolution of 10″, $P_{20/6} \approx 0.3$–0.5 in the top of the western tail and increases to 0.5–0.7 near the bottom of the western tail. In the eastern jet, $P_{20/6} \approx 0.7$ at the bright knots and ~ 0.6–0.9 along the rest of the jet. The depolarization ratio in the eastern lobe is very patchy and ranges from $P_{20/6} \approx 0.4$–0.9 in places.

vi) *Model-dependent Upper Limits to the Thermal Particle Density*

The interpretation of polarization measurements is always problematical, and the results are model dependent (see Laing 1985 for a discussion). It is possible that the position angle rotation and depolarization occur both inside the source and in a foreground screen. An upper limit to the internal RM (RM $= 800 n_e B_l L$, where n_e is the thermal electron density, B_l is the line-of-sight component of a possibly tangled ***B*** field, and L is the path length through the source) is obtained by assuming that all the depolarization is produced internally.

We will estimate the internal RM using the higher resolution (4″) data since this will minimize beam depolarization (i.e., vector averaging over RM gradients within the synthesized beam). We will also restrict ourselves to those locations where (at 4″ resolution) the observed (20, 18, and 6 cm) position angle rotation is proportional to λ^2, since this behavior is consistent with internal depolarization at low Faraday depths. The western tail is well resolved at 4″ resolution and can be approximated by the simple slab model (e.g., Burn 1966). On the other hand, the eastern jet is better approximated by an unresolved cylinder with its axis perpendicular to the line of sight (e.g., Cioffi and Jones 1980).

By fitting to the depolarization, we estimate upper limits to the internal RM in the knots in the eastern jet of ~ 30 rad m^{-2} and in the upper third of the western tail of ~ 40 rad m^{-2}. We assume the source contains uniform distributions of (tangled) ***B*** field, thermal particles, and relativistic particles. We take the line-of-sight component of the ***B*** field to be $B_l \approx B_{\min P} N^{-1/2}$, where $B_{\min P}$ is the strength of the ***B*** field at minimum pressure and N is the number of cells in the tangled field. Then, taking values of $B_{\min P}$ and L from Table 2 gives model-dependent upper limits to the internal thermal electron density of $n_e < 9 \times 10^{-4} N^{1/2}$ cm^{-3} in the eastern jet and $n_e < 2 \times 10^{-4} N^{1/2}$ cm^{-3} in the upper third of the western tail. Estimates of the value of N are very model dependent (e.g., De Young 1980; Laing 1981; Spangler 1983). Further observational and theoretical work is necessary before plausible estimates of N are available. At the moment, our parameterization of the limit on n_e reflects the current uncertainty.

f) Low-Resolution Map at 20 Centimeters

A final radio map is presented in Figure 9. It has been convolved with a clean beam of 40″ FWHM and constructed from data taken with the VLA D-array. The purpose of these observations was to determine the total length and shape of the tails.

We find that the lengths and widths quoted in § II*b* from Figure 1 do not change with the lower resolution observations. We feel confident that the largest scale sizes of structure have been properly mapped. In addition, the variation in the width down the western tail (especially the broadening to the south) and the continuous connection between the jet and eastern lobe are confirmed. Figure 9 also reveals an extension of the eastern lobe to the north, which was first noted at 20 cm and 50 cm by Robertson (1980, 1984).

III. OPTICAL FIELD OF 1919+479

a) Cluster Galaxy Distribution

A deep photographic plate of the 1919+479 field was made with the Steward Observatory 90 inch telescope in 1983 June. Using a IIIa-D emulsion behind the 140 mm direct image tube and an RG2 filter, we were able to produce a photograph covering nearly an Abell cluster diameter (~ 4 Mpc). The limiting magnitude was ~ 22 mag (in the red) for the 15 minute exposure. A total of 45 galaxies were identified on this plate with magnitudes less than 21 mag, similar to that expected for cluster membership at the redshift of 1919+479. The positions of these galaxies were measured with the two-axis Grant machine at KPNO. The resulting distribution of galaxies is shown on the low-resolution radio map in Figure 9.

Gregory and Burns (1982) noted that this cluster is rich with an equivalent Abell richness class of 0–1. It is difficult to be more specific because of the foreground stellar contamination by the Milky Way at a galactic latitude of $+15°$. The galactic latitude is also the reason why this cluster did not appear in Abell's (1958) catalog.

The distribution of the 45 measured, brightest galaxies is not symmetric, but the statistics of small numbers limits our conclusions here. There is no gross asymmetry in the projected galaxy distribution with respect to a north-south division on opposite sides of the central radio galaxy (there are 26 galaxies to the north and 18 to the south). However, the absence of galaxies in the western half of the image is quite noticeable.

In spite of the asymmetry of the projected galaxy distribution, it should be noted that there are no subcondensations visible in the galaxy distribution, such as those seen by Beers and Geller (1983) in other clusters. The 1919+479 cluster has a single core with a single, clearly dominant galaxy at its center. That is, the five to 10 brightest cluster galaxies are concentrated in a single clump which we unambiguously identify as the cluster center.

b) The Radio Galaxy: A Supergiant cD

In Figure 10 (Plate 4), a CCD frame of the central 4′ × 7′ region surrounding the radio galaxy is displayed. This image was kindly provided by F. N. Owen and R. A. White. It was made from a 1 hr exposure with the KPNO 1 m telescope

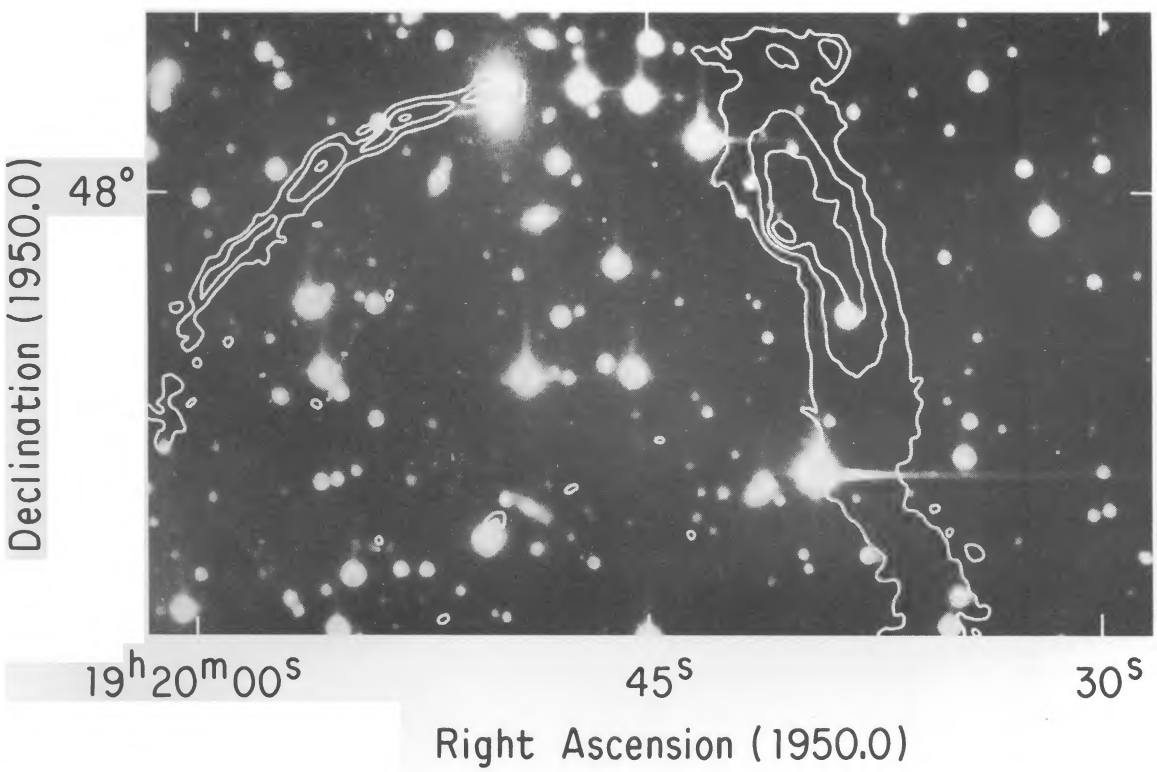

FIG. 10.—R-band CCD image of the central portion of the 1919+479 cluster. Note the extensive halo on the cD galaxy located toward the center of the frame. The image contains an overlay of the 20 cm VLA map from Fig. 1*b*.

BURNS, O'DEA, GREGORY, AND BALONEK (*see* page 82)

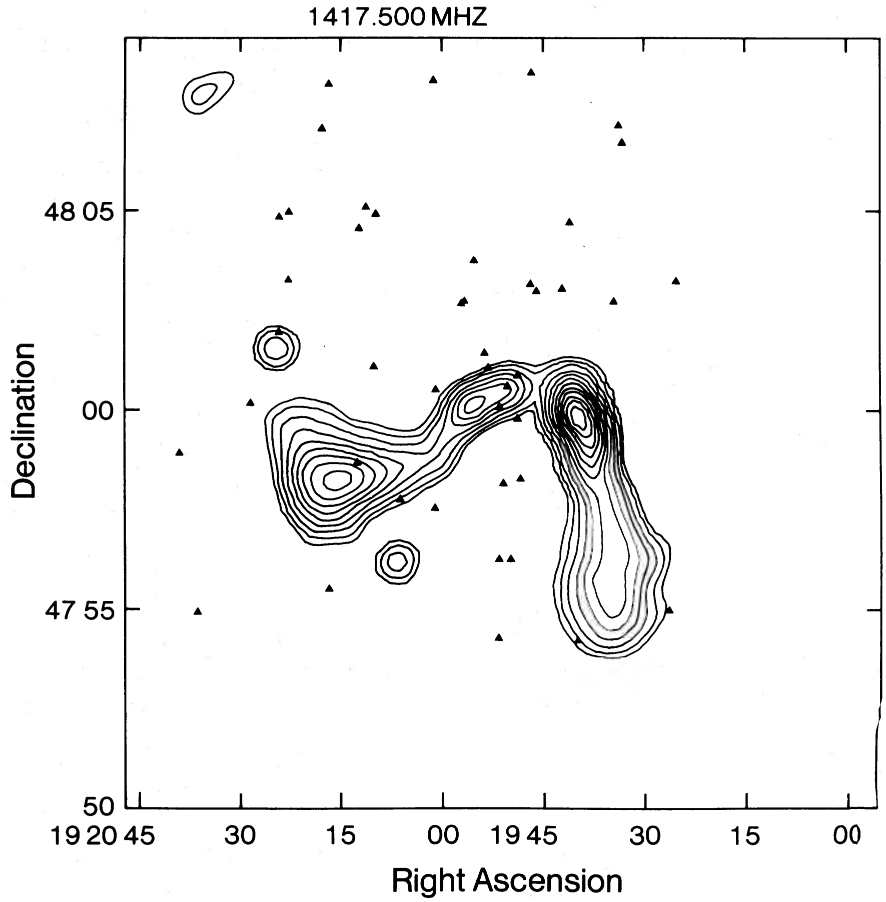

FIG. 9.—Lowest resolution VLA contour map of 1919+479. The clean beam is 40″ × 40″ FWHM. Contour levels are 1.5%, 3.0%, 6.0%, 10.5%, 16.5%, 24.0%, 33.0%, 43.5%, 55.5%, 69.0%, 84.0%, 100.5%, 118.5%, 138.0%, and 159.0% of 100 mJy per beam. The filled triangles are positions of cluster galaxies measured from a Steward Observatory 90 inch telescope plate.

using an R-band filter. There is an east-west gradient in the background of this frame because of the imperfect flat-field correction.

Figure 10 clearly shows that the galaxy associated with 1919+479 is the dominant member of the cluster. In fact, it is a full 2 mag brighter than the second brightest galaxy on the CCD frame. The absolute R magnitude measured down to the 24.5 mag arcmin^{-2} isophote (cosmologically corrected) is -23.9 (F. Owen, private communication). The halo can be traced out to ~ 230 kpc diameter along the major axis. (We note the relatively large ellipticity of this galaxy, although such ellipticities are known to exist for other cD galaxies, e.g., Carter *et al.* 1985). The light distribution in the inner ~ 50 kpc halo is well fitted by a power law with a -1.5 index, similar to that noted by Bahcall (1977) for other CD galaxies.

The above properties strongly suggest that the 1919+479 galaxy should be classified as a cD (see, e.g., Matthews, Morgan, and Schmidt 1964) and the cluster as a Bautz-Morgan (1970) class I. The galaxy is comparable in size and total brightness to the cD galaxy NGC 6166 ($M_R = -23.8$; F. Owen, private communication) in Abell 2199 (Tonry 1984). Its photometric characteristics resemble those of other first-ranked cluster galaxies recently studied by Lugger (1984). Unlike NGC 6166, NGC 7720 (3C 465; Eilek *et al.* 1984), and $\sim 45\%$ of the known cD galaxies, the 1919+479 galaxy contains only a single nucleus. Therefore, dynamical effects between nuclei within the galaxy are not responsible for shaping the radio jets or tails as suggested for other WATs in Wirth, Smarr, and Gallagher (1982). (But, see Eilek *et al.* 1984, who argue that multiple nuclei dynamical time scales are too short to produce the overall shape of the WATs.)

c) Galaxy Cluster Dynamics

Quintana and Lawrie (1982) have shown convincingly that cD galaxies have little or no motion (<100 km s^{-1}) with respect to the cluster centroids in clusters dominated by a single galaxy. Unfortunately, we do not have sufficient galaxy velocity information for the 1919+479 cluster to show this to be the case here. However, redshifts collected at KPNO using the 2.1 m telescope during the Gregory and Burns (1982) study demonstrate that the 1919+479 galaxy is part of the cluster at a redshift of 0.104. We measured the velocities of six other galaxies in the field and found them to be compatible with 1919+479.

Limits on the motion of the radio galaxy within the cluster can be set from considering the optical dominance of the cD at the center of the cluster and from the extent of the galaxy halo. First, let us assume that the cluster density distribution can be modeled by a smooth isothermal King model with a core radius of 100–200 kpc (e.g., Bahcall 1977), such as would be the case if the cluster mass is dominated by dark matter. (Note that in this model, the galaxies are merely test particles in a symmetrical background; asymmetrical galaxy distributions as in Fig. 9 could be due simply to statistical fluctuations.) Very near the core, the density is approximately a constant so that the equation of motion of the cD galaxy is that of a simple harmonic oscillator in the form

$$m_g \dot{v}_g = -4/3\pi G m_g \rho_c r \ , \tag{1}$$

where m_g and v_g are the galaxy mass and velocity, respectively, and ρ_c is the central cluster density. The solution is

$$(v_g)_{\rm rms} = r_{\rm max}(2/3\pi\rho_c G)^{1/2} \ , \tag{2}$$

where $r_{\rm max}$ is the spatial amplitude of the galaxy oscillation. Second, significant motion of the cD galaxy about the center of the cluster potential will result in stripping of the galaxy halo by the general tidal field of the cluster (Gunn 1977; Merritt 1984). The existence of the halo around the cD suggests that it is not now and never has been more than one tidal radius away from the center of the gravitational potential well. Therefore, the size of the observed galaxy halo for 1919+479 can be used to constrain the velocity of the cD. The tidal force per unit galaxy mass (acceleration) is given by

$$\Delta f = 4/3\pi G \rho_c r_g \ , \tag{3}$$

where r_g is the tidal radius of the galaxy. This must be balanced by the galaxy self-gravity, $\sim 1/2\sigma^2/r_g$ (where σ is the stellar radial velocity dispersion), appropriate for a King model with a large central concentration (Merritt 1984). Substituting ρ_c from equation (2) into equation (3) leads to a limit for the rms velocity for harmonic oscillation,

$$(v_g)_{\rm rms} = 1/2\sigma(r_{\rm max}/r_g) \ . \tag{4}$$

If the limit on $r_{\rm max}$ is given by the requirement that the cD never move more than a tidal radius from the cluster center, and $\sigma = 300$ km s^{-1} (typical for cDs; see e.g., Carter *et al.* 1985), then $(v_g)_{\rm rms} = 150$ km s^{-1}. The corresponding period is 6×10^9 yr, which is greater than the radio source lifetimes in Table 2. (Thus, the WAT structure could have been formed during a single swing through the cluster center.) This should be viewed as a conservative calculation since (1) the central potential well could be deeper than that suggested above (the extreme limit being the black pit model of Smarr and Blandford 1982) and (2) galaxy-galaxy collisions will enhance this tidal stripping effect (e.g., Richstone 1976).

We conclude that the 1919+479 radio galaxy is unlikely to be moving more than ~ 150 km s^{-1} on average in a low-amplitude harmonic oscillation about the cluster center. This conclusion must be true even if the cluster as a whole is not dynamically relaxed; otherwise, the radio galaxy would not have an extensive halo. This greatly limits the rms pressure available for bending the radio source.

d) *Comparison of the Optical and Radio Properties of 1919+479*

Also shown in Figure 10 is an overlay of the 20 cm radio map from Figure 2 onto the optical field of 1919+479. There are several interesting points worth noting.

First, the radio jets emerge from the galaxy close to a line along the minor axis (inclined by 70° with respect to the major axis).

Second, there is a faint (but real) excess of light coincident with the inner eastern jet. Could this be optical synchrotron radiation like that seen in M87 (e.g., Keel 1984) and 3C 31 (Butcher, Van Breugel, and Miley 1980)? An extrapolation of the ~ 2 mJy flux density at 20 cm for the inner jet to the optical *R* band using a spectral index of -0.5 predicts a magnitude of 25–26 mag. This is within the errors of the estimated magnitude of the excess on the CCD frame. (It is interesting to note that the radiative half-life of the relativistic electrons would be 15,000 yr, thereby constraining particle acceleration models.)

Third, there are several faint optical objects near the radio hot spot (location 7 in Fig. 1*b*) at the end of the counterjet. The positioning of the optical emission is similar to that seen on the edge of the brightened jet knot in 3C 277.3 (van Breugel *et al.* 1985*b*). We discuss this further in § V*d*.

Fourth, there is a curious alignment between an optical object and the bow which occurs in the eastern jet between points 13 and 14 in Figure 2. However, Brodie, Burns, and Bowyer (in preparation) have recently determined this to be a foreground star.

IV. X-RAY EMISSION FROM THE 1919+479 CLUSTER

a) *X-Ray Source Morphology*

Burns, Gregory, and Holman (1981) reported on the detection of a weak X-ray source coincident with the center of the 1919+479 cluster. These data were collected with the *Einstein Observatory* IPC detector (see, e.g., Giacconi *et al.* 1979 for details of the satellite imaging systems) using 2425 s of integration time. Subsequently, this field was reprocessed using improved calibration techniques and software which somewhat reduced the background noise and improved the position accuracy (point source position accuracy is now $\pm 30''$). In Figure 1*b*, the resulting reprocessed X-ray image is shown overlaid onto the VLA map which was discussed in § II. The energy range used to construct this image was 0.14–4.0 keV. The X-ray image was convolved with a circular Gaussian function of 64″ FWHM. The approximate beam size is 1′.8.

The total X-ray flux of this source is $3.5 \pm 0.9 \times 10^{-13}$ ergs cm^{-2} s^{-1} measured within a box of 4.5×3.5 arcmin^2 centered on the X-ray peak determined between the same energy limits as used for Figure 1*b*. This flux was corrected for photoelectric absorption by H I in our Galaxy using a column density of 8×10^{20} atoms cm^{-2} as determined by Heiles (1975). This flux calculation also assumed a thermal spectrum, although the final result is quite insensitive to the form of that spectrum. A background determined from an equal area region offset from any sources in the field was subtracted from the flux, and Gaussian noise statistics were assumed in computing the errors on the flux. The corresponding X-ray luminosity is 5.4×10^{42} ergs s^{-1}, which is on the low-luminosity end for Bautz-Morgan (1970) class I clusters measured by Jones and Forman (1984). There was insufficient signal in the source to determine a temperature from the IPC spectrum, so we will assume a value of 5×10^7 K throughout this discussion (typical for other cD clusters in Jones and Forman 1984).

The centroid of the X-ray emission is offset from the position of the cD galaxy by 1′.3. The emission region is also resolved (by ~ 2 beamwidths) and coincides most strikingly with the eastern jet of 1919+479. This coincidence was first noted by Harris (1982) as one of several X-ray sources which coincide with cluster radio galaxy structures.

We attempted to estimate the central density and thermal pressure of the X-ray–emitting gas by assuming an optically thin, thermal bremsstrahlung model for the emission. For simplicity, we assumed spherical symmetry within the confines of an isothermal King model (core radius 150 kpc) which, coupled with the unresolved widths of the X-ray extensions in Figure 2, will yield lower limits for these parameters. Following the procedure outlined by Burns and Balonek (1982), an estimated central density of 5.3×10^{-3} and a central pressure (nkT) of 3.6×10^{-11} is obtained for the gas near the eastern jet of 1919+479.

b) *On the Distribution and Extent of the Intracluster Medium*

The present X-ray data provide information only on the hot gas that apparently coincides with the eastern radio jet. Yet the presence of 1 Mpc extended radio emission strongly suggests that there is a much more extensive intracluster medium (ICM) which lies well outside the core of the cluster and confines the radio tails (otherwise, the radio emission would drop below detectable levels because of adiabatic expansion losses). One can use the radio emission as a probe of the presently unseen extended ICM to map out its pressure distribution (assuming an equilibrium between internal relativistic particle plus magnetic field pressure with the thermal ICM pressure). In Figure 11, the distribution of minimum internal pressure in both radio tails is shown as a function of distance from the cD galaxy.

The internal minimum pressures for the eastern radio jet (3×10^{-11} dyn cm^{-2}) are in excellent agreement with the pressure estimated from the X-ray emission. One can see, however, that the radio-tail data suggests that the general ICM pressure ($<10^{-12}$ dyn cm^{-2}) is much lower away from the eastern jet region. The resulting X-ray emissivity ($\propto P^2 1$, where P is the pressure [nkT] and 1 is the path length through the cluster) is expected to drop below the sensitivity limits of the IPC image at the distance of $\sim$400 kpc from the core on the eastern side of the source (as is observed). It is clear from Figure 11 that a continuous isothermal King model cannot fit the gas distribution near the eastern jet and the radio tails. Therefore, it appears that there are two regions of gas within the cluster: one with a high pressure (and density) near the eastern jet and a second, possibly larger region with lower pressure, which makes up the ICM like that seen in other clusters (e.g., Jones and Forman 1984).

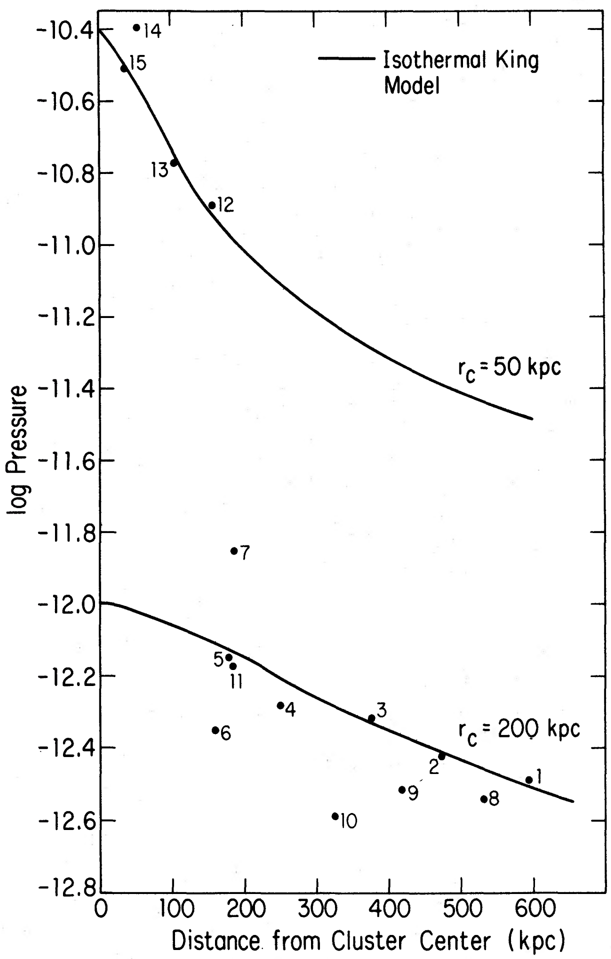

FIG. 11.—Distribution of radio source component minimum pressures as a function of distance from the radio galaxy. Curves represent best-fit isothermal King models of the gas near the eastern radio jet (*top*) and the radio tails (*bottom*). Note that both regions cannot be fitted by a single isothermal King model.

V. DISCUSSION

The observations presented in the previous three sections provide useful constraints on the models for bending the radio structure of 1919+479. We will first discuss the traditional model for bending tailed radio sources, involving dynamical pressure, and show that it is incompatible with both radio determined and optically determined parameters for the source and its environment. We then turn to a model involving collisions with relatively dense clouds in the intracluster medium. We conclude that this model is most consistent with the extensive data in §§ II–IV, and may be generally applicable to large WATs associated with cD galaxies.

a) *Dynamical Pressure Bending of a Fluid Beam*

It is often assumed that the WAT sources are straightforward extensions of NATs in which slower moving galaxies and higher momentum fluxes in the outflowing jet tail plasma produce the smaller bending angles (e.g., Miley 1980). We have applied the nonrelativistic version of this model to the eastern half of 1919+479 following the general procedure outlined by O'Dea (1985). Three equations describe the energetics of the jet, the bending of the flow, and the Mach number.

First, the luminosity of the radio jet plus tail is determined by the conversion of kinetic plus internal energy in the beam into synchrotron radiation. This is given by

$$L_E = 1/2\pi r_j^2 \rho_j v_j^3 (1 + 3/M_j^2)\epsilon , \tag{5}$$

where r_j, ρ_j, v_j, and M_j are the radius, density, velocity, and Mach number of the jet, respectively, and ϵ is the conversion efficiency. The second term in the parentheses represents the contribution of internal energy to the total energy flux. This expression can be equated with

$$L_E = L_j + L_{\rm lobe}(r_{\rm lobe}/r_j)^{2/3}(v_{\rm lobe}/v_j)^{1/3} , \tag{6}$$

where L_j and $L_{\rm lobe}$ are the observed luminosities of the jet and lobe, respectively. The terms in parentheses represent adiabatic expansion losses (or compression) which may occur during the transition from jet to lobe (e.g., Bicknell 1984). We can estimate the degree of expansion loss by assuming conservation of thrust, $\rho v^2 r^2$, and an adiabatic equation of state in the form $\rho_j/\rho_{\rm lobe} = (P_j/P_{\rm lobe})^{1/\gamma}$. For a jet flow dominated by thermal particle pressure, $\gamma = 5/3$ and

$$(L_E - L_j)/L_{\rm lobe} = (P_j/P_{\rm lobe})^{1/5} . \tag{7}$$

If the jet and lobe pressures are equal to their minimum values from Table 2 (comparing regions 8 and 11), then the above ratio is 1.2. It appears, therefore, that adiabatic expansion losses are negligible (as suggested by the spectral index data described in § II*e*[i]), possibly as a result of deceleration in the flow due to entrainment of matter (this process is represented by momentum conservation in the above). We then write $L_E = L_j + L_{\rm lobe}$.

Second, Euler's equation in the form

$$\frac{\rho_j v_j^2}{R} = \frac{\rho_{\rm ICM} v_g^2}{r_j}, \tag{8}$$

where R is the radius of curvature of a "naked" jet and v_g is the velocity of the galaxy, can be used to describe the bending of the eastern jet.

Third, the internal Mach number of the jet, defined as $M_j = [v_j^2 \rho_j/(\gamma P_j)]^{1/2}$, can be written in the form

$$M_j = \left(\frac{R}{r_j}\right)^{1/2}\left(\gamma + \frac{1}{M_g^2}\right)^{-1/2}, \tag{9}$$

where M_g is the Mach number of the radio galaxy with respect to the ICM sound speed. Equation (9) is derived from the assumption of thermal plus ram pressure confinement, and bending according to equation (8) (e.g., Begelman, Rees, and Blandford 1979; Rudnick and Burns 1981). If we assume that the large-scale curvature of the eastern jet is due to continuous dynamic pressure bending, then $R/r_j = 90''/0''.3$, leading to $M_j = 7$ if $M_g \approx 0.5$, and $M_j = 2$ if $M_g \approx 0.1$.

Combining the above three conditions on the jet and tail produces the following constraints on the galaxy velocity as a function of jet velocity:

$$v_g\left[1 + \frac{3r_j}{R}\left(\gamma + \frac{c_{\rm ICM}^2}{v_g^2}\right)\right]^{1/2} = \left(\frac{2L_E}{\pi r_j R v_j \rho_{\rm ICM}\epsilon}\right)^{1/2}, \tag{10}$$

and as a function of jet density:

$$v_g\left[1 + \frac{3r_j}{R}\left(\gamma + \frac{c_{\rm ICM}^2}{v_g^2}\right)\right]^{1/3} = \left[\frac{2\rho_j^{1/2} L_E (r_j/R)^{3/2}}{\pi r_j^2 \rho_{\rm ICM}^{3/2}\epsilon}\right]^{1/3}$$
$$= 930\ {\rm km\ s^{-1}}\left(\frac{n_j}{10^{-3}\ {\rm cm^{-3}}}\right)^{1/6}\left(\frac{\epsilon}{0.01}\right)^{-1/3}, \tag{11}$$

where $c_{\rm ICM}$ is the sound speed of the ICM (830 km s^{-1}). Note that equation (11) does not depend strongly on the powers of the jet density and reacceleration efficiency, whose values are not well known. For $L_E = 3.4 \times 10^{42}$ ergs s^{-1}, $n_{\rm ICM} = 5.3 \times 10^{-3}$ cm^{-3}, and $R/r_j = 90'/0''.3$, the roots of the cubic equation (11) were numerically determined to yield a galaxy velocity of 920 km s^{-1}.

In § III, we argued that optical data on the 1919+479 cluster constrain the cD radio galaxy to a peculiar velocity of less than 150 km s^{-1}. The cD velocity required by equation (11) is clearly inconsistent with this limit. Since v_g is such a weak function of jet density and reacceleration efficiency, our conclusion that the dynamic pressure model is inconsistent with the data is firm.

In addition, this simple model fails to account for three other structural features seen within the radio source. First, it does not explain why the bends in the eastern jet are so sharp unlike that seen in 3C 129. Second, the model has no natural explanation for the relatively abrupt transition between jet and lobe. Jones and Owen (1979) argue that the jets in NGC 1265 disrupt and form diffuse tails as they enter the turbulent wake of the supersonically moving galaxy. No such wake is expected to exist for a cD galaxy, especially at the distance of the lobe from the galaxy center (> 500 kpc). Third, this model offers no hope in explaining the western half of 1919+479. The apparent 90° bend of the counterjet to form the tail cannot be produced by the smooth pressure gradient predicted by this model.

b) Cloud Collisions and Oblique Shocks

Eilek *et al.* (1984) discussed a number of alternative models for bending the WAT source 3C 465, including buoyancy, gravitational bending, large-scale mass motions, and electrodynamic effects. They argued that each of these models has some difficulty explaining the structure of 3C 465 or is inconsistent with the radio or X-ray data or both. The same arguments can be applied to 1919+479 and so will not be repeated here. However, the last model discussed by Eilek *et al.* involving collisions with clouds in the ICM, looks attractive for 1919+479.

When a fluid jet encounters a relatively dense cloud, the resulting perturbation can propagate within the jet as an oblique shock. Such a planar shock is an effective agent for sharply bending the flow, as noted recently by Smith (1984) and Henriksen (1985). This could explain why the eastern jet of 1919+479 undergoes sharp bends rather than the continuous curvature of the NAT sources. There is evidence from both the radio and the X-ray data presented in the previous sections that the gas in the cluster is not smooth; there are significant and sudden changes both in the internal and external pressures of the radio structures, accompanied by dramatic changes in source orientation or morphology, or both. We will now argue that the overall structure of this source is consistent with cloud collisions accompanied by oblique shocks. We will elaborate upon the basic model discussed in Eilek *et al.*

First, let us consider the details of the bending of the flow associated with the eastern jet. The X-ray excess on the eastern half of the cluster shown in Figure 1*b* suggests that the jet emerges from the confines of the cD galaxy and enters into a region of the ICM which is asymmetrical and denser than average. The current X-ray data are of insufficient resolution to determine if the ICM near the jet is composed of a single ridge or a series of clouds. We will assume that the jet undergoes several "glancing blow" collisions with ICM density enhancements at regions 13 and 14.

Landau and Lifshitz (1982, § 86) present an articulate discussion on refraction of a supersonic fluid flow by a planar shock front inclined at an angle with respect to the initial flow direction (see also Stocke, Burns, and Christiansen 1985). Such a configuration is expected from an off-center collision of a radio jet with an intracluster cloud. The upstream Mach number of the jet can be shown to be related to the jet bending angle, ψ (measured from a line oriented along the initial flow direction), and the ratio of the shock to upstream pressures (P_2/P_1) via the following somewhat lengthy but very useful expression:

$$M_{j,1}^2 = \frac{\xi - 2\gamma}{\xi\gamma(\gamma+1)^2}(\xi - 2\gamma)\cot^2\Psi + \xi(\gamma+1)$$
$$\pm \cot\Psi[(\xi - 2\gamma)^2\cot^2\Psi + 2(\xi - 2\gamma)\xi(\gamma+1) - \xi^2(\gamma+1)^2]^{1/2}, \tag{12}$$

where $\xi = (\gamma + 1)P_2/P_1 + (\gamma - 1)$, and γ is the ratio of specific heats (again taken to be 5/3). The two solutions indicate a supersonic or subsonic flow behind the shock. If the jet is assumed to remain in equipartition through the shock front, then the ratio of the pressures can be written as $(S_2/S_1)^{4/7}$, where S is the observed flux density (this ratio is ~ 15 for knot 13). These pressures, combined with an observed bending angle of 20°, lead to a pair of Mach numbers equaling 3.1, 2.1. The downstream Mach number, $M_{j,2}$, can be shown to be 1.7, 0.8.

The actual bending of the jet can again be modeled using Euler's equation. The pressure gradient responsible for deflecting the jet results from the compression of ICM cloud material by an external shock formed during the supersonic jet/cloud collision (analogous to the hot spot formation at the working surface of classical doubles). The pressure gradient is sharp because of the shock front and is assumed to extend over an equivalent jet width. Therefore, Euler's equation for a nonrelativistic jet can be written as

$$\frac{\rho_j v_j^2}{R} = \frac{P_{\rm shock}}{r_j}, \qquad (13)$$

where $P_{\rm shock}$ is taken to be the minimum internal pressure of the radio knot 13 (3.6×10^{-11} dyn cm^{-2}), in Table 2. Combining equations (5), (12), and (13) leads to the following relationships of jet velocity and density with radiation efficiency:

$$v_j = \frac{2L_E}{\pi\gamma\epsilon P_{\rm shock} r_j R(1 + 3/M_j^2)}, \qquad (14)$$

$$n_j = \frac{\pi^2\epsilon^2\gamma^3 r_j R^3 P_{\rm shock}^3(1 + 3/M_j^2)}{4L_E^2 m_p};$$

R/r_j is $\approx 20''/0''.3$ (where the radius of curvature of the jet, R, is now measured for the sharper bend in knot 13), $M_j = 3.1$, and m_p is the proton mass. Using these values, the constraints in equations (14) are graphically illustrated in Figure 12. For efficiencies of 1%–10%, the density of the jet is 10^{-5}–10^{-3} cm^{-3}. These densities are consistent with that expected if some portion of the radio depolarization [§ II*e*(v)] is due to thermal material in the jet.

Next, the transition from jet to lobe in the eastern half of 1919+479 might be explained by the emergence of the jet from a relatively high pressure to low pressure region. As discussed in § IV, the X-ray pressure near the eastern jet is consistent with the minimum internal pressure of the radio jet. As the jet emerges from the X-ray ridge, it loses collimation, and the pressure drops dramatically (from a high of 4×10^{-11} dyn cm^{-2} in knot 14 to 2×10^{13} dyn cm^2 at position 8 in the lobe). The jet may have become violently unstable, disrupted, and flared outward to produce the eastern lobe. In fact, Kelvin-Helmholtz or hose instabilities (see, e.g., Hardee 1984; Norman *et al.* 1985) may have begun to grow earlier in the flow triggered by the perturbations from the cloud collisions; there is a strong suggestion of a "wiggle" superposed upon the sharp bends in the jet in Figure 4. Payne and Cohn (1985) have shown that if the velocity of the jet drops below the sum of the internal plus external sound speeds then the jet becomes unstable. Such a situation may arise in the eastern jet of 1919+479 as a result of entrainment of matter, increase in temperature from the cloud to the general ICM, or from the shock geometry (i.e., subsonic solution for downstream flow described above). The spectral index data are also consistent with a transition to a subsonic flow (i.e., there is no flat spectrum hot spot at the end of the lobe).

We conclude, therefore, that collisions of the eastern jet within a clumpy ICM are consistent with the radio, X-ray, and

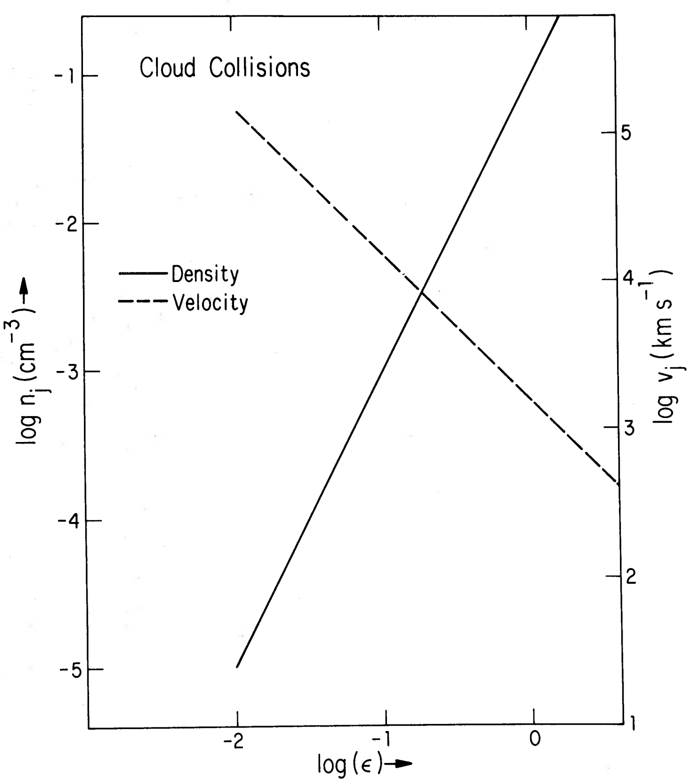

FIG. 12.—Predicted relations between jet density, velocity, and reacceleration efficiency for a jet/cloud collision (oblique shock) model

optical data. Unlike the dynamic pressure models, extreme galaxy velocities or unphysical jet parameters are not required. We now must ask if a similar model can explain the peculiar morphology of the western half of 1919+479.

c) *The Western Counterjet*

The counterjet on the western side of the cD galaxy is not as well defined as the eastern jet because of the lower surface brightness. Nonetheless, it appears that the counterjet makes a very abrupt transition to a tail, oriented perpendicular to the counterjet at position 7 in Figure 1*b* (see also Fig. 2). What happens to the flow of radio plasma in the jet/tail transition? As discussed by Burns (1981), it is unlikely that the jet plasma simply comes to rest. In this picture, the tail would be produced by motion of the galaxy leaving behind a radio wake (e.g., Jaffe and Perola 1974). The large size of the radio source requires an average galaxy velocity of ~ 8000 km s^{-1} relative to the ends of the tails (i.e., 0.8 Mpc per 10^8 yr). If particle acceleration occurs, then the age determined via the spectral steepening is increased and the required velocity is decreased. However, unlike the eastern lobe, there is no evidence for *in situ* particle acceleration in the western tail.

Can the above velocity be due to the tails drifting buoyantly southward through the ICM? The terminal velocity of such a drift is of order

$$v_t = \left(\frac{GM_c\, r_{\rm tail}}{R_c^2}\right)^{1/2} , \tag{15}$$

where $r_{\rm tail}$ is the tail radius and M_c is the cluster mass at distance R from the cluster center (see, e.g., Cowie and McKee 1975). For conservative cluster parameters of $M_c \approx 10^{14}\ M_\odot$ within 500 kpc of the cluster center and $r_{\rm tail} = 100$ kpc, then $v_t \approx 300$ km s^{-1}. This velocity is too low to produce the extended western tail in 1919+479 even allowing for particle acceleration (due to insufficient kinetic energy in the flow).

Thus, the material in the western tail must have a directed velocity in excess of that produced by buoyancy alone. This means that the hot spot (7) in Figure 1 does not stop the beam fluid but rather *redirects* it to the south with a velocity greater than 8000 km s^{-1}. The cloud collision model discussed in § V*c* above could potentially explain the 90° bending of the flow, as well as providing a unified model for the two sides of 1919+479.

Such a sharp bend (which could be exagerated by projection effects) requires a much "harder" collision than the "glancing blow" model discussed in § V*c*. Possibly a head-on collision with a denser cloud would serve our needs here. The nature of this cloud is discussed in § V*e* below.

The counterjet cannot coherently bend by 90° via a single oblique shock. Landau and Liftshitz (1982) show that the maximum bending angle for a fluid refracted by a planar shock is

$$\Psi_{\rm max} = \sin^{-1}(1/\gamma) = 37° \tag{16}$$

for $\gamma = 5/3$. Therefore, some other mechanism or interaction with the cloud must be invoked. Two possibilities come to mind. First, as suggested from equation (16), the counterjet does not remain collimated when it collides with a very dense cloud (which acts like a "brick wall") oriented at a large angle to the flow direction. The flow simply "splashes" off the cloud to the south enlarging in cross section to form the western tail. It eventually comes into pressure equilibium with the surrounding ICM. In the process of reaching equilibrium, the tail may overexpand and "bounce" or recollimate as suggested by Sanders (1983) for radio jets. This could explain the profile width distribution in Figure 3. Second, the jet may inflate a hot cavity on the southern edge of the cool cloud. The thermalized flow may eventually break through the wall to the south (path of least resistance), again forming the radio tail. This is somewhat similar to the model of Lonsdale and Barthel (1984) which attempts to explain double hot spots in radio lobes and to the "cloud rupture" model of Henricksen (1985).

Independent of the details of the jet/cloud interaction, one can make several predictions concerning the counterjet within the basic framework of this model. Differences between the jet and counterjet could be due to differences in their environments. Let us assume that intrinsically identical and dissipationless jets emerge from the "engine" at the core of 1919+479. Three fundamental quantities are conserved on either side. First, the equation of state takes the form

$$P_{\rm cj}/P_j = (S_{\rm cj}/S_j)^{4/7} = (n_{\rm cj}/n_j)^\gamma , \tag{17}$$

where we again assume minimum pressure (equipartition) conditions and an ideal gas. Since $S_{\rm cj}/S_j \approx 1/50$, the density of the counterjet is $n_{\rm cj} = 0.26 n_j$.

Second, energy conservation in the form

$$\frac{1}{2}v_{\rm cj}^2 + \frac{\gamma}{\gamma-1}\frac{P_{\rm cj}}{\rho_{\rm cj}} = \frac{1}{2}v_j^2 + \frac{\gamma}{\gamma-1}\frac{P_j}{\rho_j} \tag{18}$$

suggests that $v_{\rm cj} = v_j$ for cold, supersonic jets.

Third, mass flux conservation in the form

$$n_{\rm cj}\, v_{\rm cj}\, r_{\rm cj}^2 = n_j v_j r_j^2 \tag{19}$$

predicts an average counterjet radius (currently unmeasurable because of poor S/N) of $2r_j$. This is still much smaller than the hotspot at position 7 in Figure 1 (radius is 4."4).

If the jets are in pressure balance with their surroundings, then the lower ICM pressure near the western jet in comparison to that of the eastern jet will cause the western jet to suffer greater adiabatic expansion losses and, therefore, will be less bright. However, such expansion losses are recoverable at the westernmost hot spot, and can produce a tail of brightness equal to the eastern tail, as is observed.

d) *Nature of the ICM Clouds*

The radio, X-ray, and optical imaging data can be used to constrain the clouds which bend the radio jets. First, if we assume that a cloud moves less than a distance D during the $\tau \approx 10^8$ yr lifetime of 1919+479 (accelerated by ram pressure), then the mass of the cloud is

$$M_{\rm cl} > \frac{\rho_j v_j^2 \pi r_j^2 \tau^2}{D} . \tag{20}$$

For $n_j \approx 10^{-4}$ cm^{-3}, $v_j \approx 1.6 \times 10^4$ km s^{-1}, $r_j = 0."6$ (counterjet radius), and $D \approx 4r_j$ (i.e., the cloud moves no more than several jet diameters), $M_{\rm cl} > 2.5 \times 10^9\ M_\odot$.

Second, the cloud can be heated by the turbulent interaction with the plasma beam (e.g., Eilek 1979). Following Eilek *et al.* (1984), the balance of the volume-heating rate with the cooling rate (for an optically thin gas of cosmic abundance) yields a limit on the density of the cloud,

$$n_{\rm cl}^2 \approx \frac{\epsilon_H/\epsilon L_E}{4/3\pi r_{\rm cl}^3 f\Lambda(T)} , \tag{21}$$

where ϵ_H is the fraction of jet energy flux which goes into heating, f is the volume filling factor, r_{cl} is the cloud radius, and $\Lambda(T)$ is the cooling function (Raymond, Cox, and Smith 1976). Combining equations (20) and (21), eliminating r_{cl}, produces an estimate of the cloud density in the form

$$n_{cl} \approx \frac{\epsilon_H/\epsilon L_E m_p D}{\pi r_j^2 \tau^2 f \Lambda(T) \rho_j v_j^2}$$

$$\approx 0.01 \text{ cm}^{-3} \left\{ \left(\frac{\epsilon_H}{\epsilon} \right) f^{-1} \left[\frac{\Lambda(T = 10^6 \text{ K})}{10^{-22} \text{ ergs cm}^{-3} \text{ s}^{-1}} \right]^{-1} \right\} . \quad (22)$$

If these clouds are in pressure balance with the surrounding ICM, then the temperature of the cloud will be given by $T = P/(n_{cl} k)$. For the counterjet/cloud interaction in the western half of 1919+479, the ICM pressure near region 7 (Fig. 1*b*) from the King model fit (Fig. 11) ($P \approx 8 \times 10^{-13}$ dyn cm^{-2}) implies a temperature of 6×10^5 K. These parameters correspond to a cloud radius of 13 kpc (8″). The uncertainties in the parameters entering into equation (22), especially ϵ_H/ϵ, f, and M_{cl}, could raise or lower the cloud density (and temperature) by a factor of 10. In the dense cloud case, optical Hα emission, for example, may be possible especially if the density increases because of thermal instabilities (produced by the cloud/jet interaction).

Might one of the faint optical objects near the hot spot (region 7) in Figure 8 be such an Hα cloud? There are several possible examples in other environments. Graham and Price (1981) reported the presence of optical emission line clouds near the middle lobe ($\sim$35 kpc from the core) of Cen A. Brodie, Bowyer, and McCarthy (1985) and van Breugel *et al.* (1985*a*) have claimed that Minkowski's object in Abell 194 is the site of the collision between a radio jet and a cool cloud in the ICM. Similarly, there is excellent evidence from optical and radio data that the jet in 3C 277.3 is bent by a cloud collision and resulting oblique shock (van Breugel *et al.* 1985*a*). On the other hand, O.Dea, Owen, and Keel (1986) have failed to detect optical emission from such clouds near sharp bends in 3C 465. A recent Hα CCD image of the 1919+479 field by Brodie, Burns, and Bowyer (1986) indicates that one of the optical images near the western radio jet is an emission-line object at the redshift of the cluster.

The eastern jet bending requires a less severe cloud collision. The pressure of the surrounding ICM (Fig. 11), 3.6×10^{-11} dyn cm^{-2}, coupled with a density of $\sim 10^{-2}$ cm^{-3} (from eq. [22]) requires $T = 3 \times 10^7$ K (for thermal confinement). This produces radiation in the IPC X-ray band and could account for the enhanced X-ray emission on the eastern half of the cluster. In this case, the "glancing blow" collision with ICM clouds heated and compressed the gas but not enough to produce thermal instabilities.

The constraints on the nature of the ICM clouds from jet/cloud interactions are, at present, very broad. One can conceive of situations where such clouds are effectively invisible. There is a dearth of optical emission lines from gases with $T \approx 10^6$–10^7 K (e.g., Raymond *et al.* 1976). The uncertainties and variations in jet/cloud conditions illustrated in equation (22) could allow ICM clouds in this temperature range, effectively hiding them from detection (possibly as in the case of 3C 465?). Alternatively, these clouds could radiate prodigiously at optical or X-ray wavelengths.

VI. SUMMARY AND CONCLUDING REMARKS

The new VLA data on 1919+479 presented in this paper have revealed a complexity of structure on a wide variety of scale sizes ranging from regularly spaced knots (<0″.3 radius) in the eastern jet to a diffuse tail-lobe with a spectral index gradient. Two features are of particular importance in modeling the overall bending of the source. First, *the eastern jet does not bend continuously but instead bends sharply at several knots.* This differs from the smoothly curving jets seen in the lower luminosity, narrow-angle tailed sources, but may be a common property among WATs. Second, the newly discovered western counterjet ends abruptly at a "hot spot." The much broader western tail begins in this vicinity but is oriented orthogonally (on the plane of the sky) to the counterjet. Both properties suggest an impulsive bending of the jets rather than a continuous curvature bending. (We use "impulsive" here to describe a mechanism that produces a sharp, transverse change in the jet flow direction.)

The CCD image of the cD galaxy associated with 1919+479 reveals an extensive galaxy halo more than 230 kpc in diameter. Limits on the tidal stripping of this halo by the general cluster field suggest that the galaxy cannot move more than $\sim$150 km s^{-1} over a distance which is given by the tidal radius. This agrees with statistical velocity data compiled for other rich cluster cD galaxies (e.g., Quintana and Lawrie 1982). There is insufficient dynamic pressure to bend the jets in a manner consistent with the tail energetics, and this mechanism is nonimpulsive.

The *Einstein* IPC X-ray image of the cluster shows that the ICM near 1919+479 is clumpy. There is a particular concentration of hot gas surrounding the eastern jet. Collisions with these clumps of intergalactic gas might naturally supply the impulsive force necessary to sharply bend (and decollimate) the radio jets.

Should one generalize a cloud collision model to explain the bending of all WATs? Not all WATs are associated with cD galaxies and with clusters containing a single concentration of galaxies. In these other environments, dynamic pressure may play a larger role either resulting from direct galaxy motion or dynamical interactions of subcondensations within the clusters. Such examples include NGC 4874, one of two giant ellipticals in the Coma cluster (O'Dea and Owen 1985; Feretti and Giovannini 1985), and NGC 2329 in Abell 569 (Feretti *et al.* 1985), associated with one of two main concentrations of galaxies. Both sources are small ($\sim$50 kpc diameter) with diffuse lobes. The energy requirements in these sources, therefore, are less severe.

On the other hand, there is a subset of WATs associated with cD galaxies. Here, the bending constraints are more demanding. About 25% of cD galaxies have radio emission with flux densities above 200 mJy at 20 cm (Burns, White, and Hough 1981). In a statistical sample of Abell clusters with distance class less than 3, only 12% ($\frac{1}{8}$) of the radio-loud cDs with extended emission have noncolinear WAT morphology (Owen, Burns, and White 1986). Within the framework of the cloud collision model, this fraction describes the probability of bending radio jets/tails via cloud collisions. In addition, some WATs, such as that in A690 (Burns 1986), have S-shaped symmetry, as would be expected by random cloud collisions.

The probability of jet/cloud collisions will increase with the linear extent of the radio jets and tails. Therefore, the largest WATs should be the best to search for such interactions. Indeed, the larger WATs ($\sim$1 Mpc sized) are more asymmetrical, as would be expected with random cloud collisions, than the intermediate sized ($\sim$200 kpc) WATs (such as 3C 465). Further observations of a larger complete sample of WATs at a variety of wavelengths (i.e., radio, optical, and X-ray) are needed to rigorously test this suggestion.

The authors are grateful to M. Norman for his illuminating discussions on jet hydrodynamics and his comments on the manuscript, to D. Clarke for his help with equation 12, to D. Harris for his aid in interpreting the X-ray data and his comments on the paper, to C. MacCallum for his help on early VLA data reductions, to J. Stocke for his assistance in obtaining the photographic plate at Steward Observatory, to F. Owen for obtaining and interpreting the CCD frame, and to an anonymous referee for improving the theoretical discussion. J. O. B. was supported in this work by NSF grant AST83-13558 and NASA's *Einstein* guest investigator program grant NAG8-450; S. A. G. was also partially supported by NSF grant AST83-12791.

REFERENCES

Abell, G. O. 1958, *Ap. J. Suppl.*, **3**, 211.
Baars, J. W. M., Genzel, R., Pauliny-Toth, I. I. K., and Witzel, A. 1977, *Astr. Ap. Suppl.*, **61**, 9.
Bahcall, N. A. 1977, *Ann. Rev. Astr. Ap.*, **15**, 505.
Bautz, L. P., and Morgan, W. W. 1970, *Ap. J. (Letters)*, **162**, L149.
Beers, T. C., and Geller, M. J. 1983, *Ap. J.*, **274**, 491.
Begelman, M. C., Rees, M. J., and Blandford, R. D. 1979, *Nature*, **279**, 770.
Bicknell, G. V. 1984, *Ap. J.*, **286**, 68.
Bridle, A. H. 1982, in *IAU Symposium 97, Extragalactic Radio Sources*, ed. D. Heeschen and C. Wade (Dordrecht: Reidel), p. 121.
Bridle, A. H., and Perley, R. A. 1984, *Ann. Rev. Astr. Ap.*, **21**, 319.
Brodie, J. P., Bowyer, S., and McCarthy, P. 1985, *Ap. J. (Letters)*, **293**, L59.
Brodie, J. P., Burns, J. O., and Bowyer, S. 1986, in preparation.
Burns, B. J. 1966, *M.N.R.A.S.*, **133**, 67.
Burns, J. O. 1981, *M.N.R.A.S.*, **195**, 523.
———. 1983, in *Astrophysical Jets*, ed. A. Ferrari and A. G. Pacholczyk (Dordrecht: Reidel), p. 67.
———. 1986, *Canadian J. Phys.*, in press.
Burns, J. O., and Balonek, T. J. 1982, *Ap. J.*, **263**, 546.
Burns, J. O., Eilek, J. A., and Owen, F. N. 1982, in *IAU Symposium 97, Extragalactic Radio Sources*, ed. D. S. Heeschen and C. M. Wade (Dordrecht: Reidel), p. 45.
Burns, J. O., Gregory, S. A., and Holman, G. D. 1981, *Ap. J.*, **250**, 450.
Burns, J. O., and Owen, F. N. 1979, *A.J.*, **84**, 1478.
Burns, J. O., Owen, F. N., and Rudnick, L. 1978, *A.J.*, **83**, 312.
Burns, J. O., White, R. A., and Hough, D. H. 1981, *A.J.*, **86**, 1.
Butcher, H. R., van Breugel, W. J. M., and Miley, G. K. 1980, *Ap. J.*, **235**, 749.
Carter, D., Inglis, I., Ellis, R. S., Efstathiou, G., and Godwin, J. G. 1985, *M.N.R.A.S.*, **212**, 471.
Cioffi, D. F., and Jones, T. W. 1980, *A.J.*, **85**, 368.
Clark, B. G. 1980, *Astr. Ap.*, **89**, 377.
Cowie, L., and McKee, C. 1975, *Astr. Ap.*, **43**, 337.
Dennison, B. 1979, *A.J.*, **84**, 725.
De Young, D. S. 1980, *Ap. J.*, **241**, 81.
Eilek, J. A. 1979, *Ap. J.*, **230**, 373.
Eilek, J. A., Burns, J. O., O'Dea, C. P., and Owen, F. N. 1984, *Ap. J.*, **278**, 37.
Feretti, L., and Giovannini, G. 1985, *Astr. Ap.*, **147**, L13.
Feretti, L., Giovannini, G., Gregorini, L., Padrielli, L., Roland, J., and Valentijn, E. A. 1985, *Astr. Ap.*, **147**, 321.
Giacconi, R., *et al.* 1979, *Ap. J. (Letters)*, **234**, L1.
Graham, J. A., and Price, R. M. 1981, *Ap. J.*, **247**, 813.
Gregory, S. A., and Burns J. O. 1982, *Ap. J.*, **255**, 373.
Gunn, J. E. 1977, *Ap. J.*, **218**, 592.
Hardee, P. E. 1984, *Ap. J.*, **277**, 106.
Harris, D. 1982, in *IAU Symposium 97, Extragalactic Radio Sources*, ed. D. S. Heeschen and C. M. Wade (Dordrecht: Reidel), p. 77.
Heiles, C. 1975, *Astr. Ap. Suppl.*, **20**, 37.
Henriksen, R. 1985, in *Physics of Energy Transport in Extragalactic Radio Sources*, ed. A Bridle and J. Eilek (*Proc. NRAO Workshop* No. 9), p. 122.
Hjellming, R. M., ed. 1982, *An Introduction to the NRAO Very Large Array* (NRAO).
Jaffe, W. J., and Perola, G. C. 1973, *Astr. Ap.*, **26**, 423.
Jones, C., and Forman, W. 1984, *Ap. J.*, **276**, 38.
Jones, T. W., and Owen, F. N. 1979, *Ap. J.*, **234**, 318.
Keel, W. C. 1984, *Ap. J.*, **279**, 550.
Laing, R. 1981, *Ap. J.*, **248**, 87.
———. 1985, in *Proc. NRAO Workshop 9: Physics of Energy Transport in Extragalactic Radio Sources*, ed. A. Bridle and J. Eilek (NRAO), p. 90.
Landau, L. D., and Lifshitz, E. M., 1982, *Fluid Mechanics* (New York: Pergamon).
Lonsdale, C. J., and Barthel, P. D. 1984, *Astr. Ap.*, **135**, 45.
Lugger, P. M. 1984, *Ap. J.*, **286**, 106.
Matthews, T. A., Morgan, W. W., and Schmidt, M. 1964, *Ap. J.*, **140**, 35.
Merritt, D. 1984, *Ap. J.*, **276**, 26.
Meyers, S. T., and Spangler, S. R. 1985, *Ap. J.*, **291**, 52.
Miley, G. 1980, *Ann. Rev. Astr. Ap.*, **18**, 165.
Norman, M. L., Smarr, L., and Winkler, K.-H. 1985, in *Numerical Astrophysics*, ed. J. Centrella, J. LeBlanc, and R. Bowers (Boston: Jones & Bartlett), p. 88.
O'Dea, C. P. 1985, *Ap. J.*, **295**, 80.
———. 1986, *Ap. J.*, **301**, 84.
O'Dea, C. P., and Owen, F. N. 1985, *A.J.*, **90**, 927.
O'Dea, C., Owen, F. N., and Keel, W. 1986, *Canadian J. Phys.*, in press.
Owen, F. N., Burns, J. O., and White, R. A. 1986, in preparation.
Owen, F. N., and Rudnick, L. 1976, *Ap. J. (Letters)*, **205**, L7.
Payne, D., and Cohn, H. L. 1985, *Ap. J.*, **291**, 655.
Quintana, H., and Lawrie, D. G. 1982, *Ap. J.*, **87**, 1.
Raymond, J. C., Cox, D. P., and Smith, B. W. 1976, *Ap. J.*, **204**, 290.
Richstone, D. O. 1976, *Ap. J.*, **204**, 642.
Robertson, J. G. 1980, *Nature*, **286**, 579.
———. 1984, *Astr. Ap.*, **138**, 41.
Rudnick, L., and Burns, J. O. 1981, *Ap. J. (Letters)*, **246**, L69.
Sanders, R. H. 1983, *Ap. J.*, **266**, 73.
Schwab, F. R. 1980, *Proc. SPIE*, **231**, 18.
Simard-Normandin, M., and Kronberg, P. P. 1980, *Ap. J.*, **242**, 74.
Simard-Normandin, M., Kronberg, P. P., and Button, S. 1981, *Ap. J. Suppl.*, **45**, 97.
Smarr, L., and Blandford, R. 1982, preprint.
Smith, M. D. 1984, *M.N.R.A.S.*, **211**, 767.
Spangler, S. 1983, *Ap. J. (Letters)*, **271**, L49.
Stocke, J., Burns, J. O., and Christiansen, W. 1985, *Ap. J.*, **299**, 799.
Thompson, A. R. 1982, in *Synthesis Mapping*, ed. A. R. Thompson and L. R. D'Addario (*Proc. NRAO-VLA Workshop*), p. 5–1.
Thompson, A. R., Clark, B. G., Wade, C. M., and Napier, P. J. 1980, *Ap. J. Suppl.*, **44**, 151.
Tonry, J. L. 1984, *Ap. J.*, **279**, 13.
Valentijin, E. A. 1981, ESO preprint No. 172.
Vallée, J. P., and Bignell, C. 1983, *Ap. J.*, **272**, 131.
van Breugel, W., Filippenko, A. V., Heckman, T., and Miley, G. 1985*a*, *Ap. J.*, **293**, 83.
van Breugel, W., Miley, G., Heckman, T., Butcher, H., and Bridle, A., 1985*b*, *Ap. J.*, **290**, 496.
Wardle, J. F. C., and Kronberg, P. P. 1974, *Ap. J.*, **194**, 249.
Wirth, A., Smarr, L., and Gallagher, J. S. 1982, *A. J.*, **87**, 602.

THOMAS J. BALONEK: Department of Physics and Astronomy, Colgate University, Hamilton, NY 13346

JACK O. BURNS and STEPHEN A. GREGORY: Institute for Astrophysics, University of New Mexico, Albuquerque, NM 87131

CHRISTOPHER P. O'DEA: National Radio Astronomy Observatory, Edgemont Road, Charlottesville, VA 22903